Mineralium Deposita
https://doi.org/10.1007/s00126-026-01441-8

ARTICLE

Burbankite-bearing ferrocarbonatite and its alteration to LREE ore at Swartbooisdrift, NW Namibia

Albert Riehm[1] · Kirsten Drüppel[1] · Lars Lenhart[1] · Regina Mertz-Kraus[2] · Rainer Ellmies[3]

Received: 30 September 2025 / Accepted: 18 February 2026

Abstract

Based on compiled mineralogical and geochemical data, we show that burbankite-rich ferrocarbonatite is altered to calcite–bastnäsite–monazite ore at Swartbooisdrift, NW Namibia. The magmatic carbonatite assemblage comprises ankerite, magnetite, pyrochlore, fluorapatite, and locally abundant burbankite. All of these minerals can be enriched in layers that define a magmatic flow banding. Burbankite formation can be restrained to ~ 650 °C. Late-magmatic to hydrothermal alteration proceeds in situ from burbankite to carbocernaite (I to II) ± calcite ± barite ± strontianite, then cordylite-(Ce), monazite-(Ce) and finally ancylite-(Ce). Pyrochlore alters to columbite-(Fe) and fluorapatite to secondary monazite-(Ce). The calcite–bastnäsite–monazite ore forms below ~ 460 °C as veins, lenses and bands confined to the main ferrocarbonatite dikes. Its pinkish color results from minor hematite. Mass-balance calculations indicate fluid-assisted removal of Sr, Na, Mg, Ba and addition of Ca, P, Fe, Mn and LREE with modest volume loss to reach ore grades. C-O stable isotope analyses for the ferrocarbonatite, burbankite and LREE ore show an increasingly heavier $\delta^{18}O$ signature linked to the hydrothermal alteration with an interpreted rising crustal influence and decreasing temperatures. Additionally, in-situ trace element analysis further provides arguments for the hydrothermal character of LREE redistribution through fluid-sensitive element ratios (Th/U; Y/Ho; Pb/Th). Our data suggest that formation of the Swartbooisdrift LREE ore results from instability and reaction of early Na-carbonates, apatite, and pyrochlore with progressive fluid evolution (decreasing Na and increasing oxygen fugacity with decreasing T), finally leading to a transformation of burbankite-rich zones of ferrocarbonatite into pink ore along carbonatite-hosted structures. This establishes a coherent magmatic–hydrothermal pathway from primary burbankite to economic LREE mineralization.

Keywords Carbonatite · Burbankite · Ankerite · Namibia · REE · Alteration · Fractionation

Introduction

Rare earth elements (defined for the purposes of this paper as Y, La–Lu and abbreviated REE/REEs) are critical raw materials of growing strategic importance (International Energy Agency, Global Critical Minerals Outlook 2025). The majority of REE deposits, particularly those containing light REEs (LREEs, La–Nd, rarely Sm), are closely associated with carbonatites and alkaline igneous rocks, which can also harbor substantial quantities of other industrially significant metals, such as Nb, P, and F (Wang et al. 2020).

Despite increasing interest in carbonatite-related LREE deposits, the mechanisms of REE concentration remains debated (Anenburg et al. 2020; Louvel et al. 2022; Yuan et al. 2024; Reece et al. 2025). Carbonatite-related LREE deposits are mostly a feature of primary-magmatic LREE enrichment, many are hydrothermally upgraded, and some are volumetrically condensed through weathering and therefore enriched (Andersen et al. 2017). In the magmatic stage the main LREE carriers are apatite, monazite, pyrochlore, and carbonates. The principal LREE carbonate, proposed to crystallize directly from strongly fractionated and Na-rich

Editorial handling: K. Kelley

✉ Albert Riehm
albert.riehm@kit.edu

[1] Department of Mineralogy and Petrology, Institute of Applied Geosciences, Karlsruhe Institute of Technology (KIT), Karlsruhe, Germany

[2] Institute of Geosciences, Johannes Gutenberg-University Mainz, J.-J.-Becher-Weg 21, 55128 Mainz, Germany

[3] Gecko Exploration (PTY) Ltd./Ondoto Rare Earth (PTY) Ltd., Windhoek, Namibia

Published online: 16 March 2026

carbonatite magma, is burbankite, a mineral that is rarely preserved in most carbonatites (Zaitsev et al. 2002; Wall et al. 2004; Anenburg et al. 2020; Chakhmouradian and Dahlgren 2021; Nikolenko et al. 2022). Instability of burbankite during late magmatic to hydrothermal conditions, linked with decreasing alkalinity, in the first stage leads to pseudomorphic replacement with carbocernaite, REE-(fluor)carbonates, ancylite-(Ce), and monazite-(Ce) in some cases conserving the euhedral hexagonal shape (Zdorik 1966; Zaitsev et al. 1998; Belovitskaya and Pekov 2004; Wall et al. 2004; Broom-Fendley et al. 2016; Sitnikova et al. 2021). Secondary alteration processes can be pervasive to the extent of complete obliteration of primary textures as described for example for Kangankunde, Malawi (Wall and Mariano 1996; Broom-Fendley et al. 2017; Chikanda et al. 2019) and Wigu Hill (Moshi et al. 2024). Raman spectroscopy has been employed increasingly for the identification of the complex and µm-scaled mineralogy of carbonatites and especially for REE-(fluor)carbonates (Chakhmouradian and Dahlgren 2021; Sitnikova et al. 2021; Sidorov et al. 2024).

This study presents important insights to some of these mechanisms by investigating ferrocarbonatites from Swartbooisdrift (NW Namibia). Both rare primary burbankite, pyrochlore and fluorapatite are preserved in an ankerite matrix. Alteration assemblages and complete pseudomorphs are observable in sequence. New mineralogical and geochemical data with results from previous studies (Seckendorff et al. 2000; Drüppel 2003; Drüppel et al. 2005, 2007; Leible and Drüppel 2014) and recent exploration datasets from Ondoto Rare Earth (Pty) Ltd (Ellmies et al. 2021) are compiled. We establish (i) the paragenesis from magmatic to hydrothermal REE-rich assemblages, (ii) constrain physicochemical conditions responsible for formation and transformation of phases such as burbankite, and (iii) evaluate pathways and extents of LREE mobility. Our results define a magmatic–hydrothermal process in which early burbankite-rich domains in ferrocarbonatite are progressively altered and finally transformed into calcite–bastnäsite–monazite ore, which is confined to the carbonatite dikes.

Geological overview

Regional geology

The study area is in NW Namibia close to the settlement Swartbooisdrift at the Kunene River (Fig. 1). The oldest lithology in the region is the Proterozoic Epupa Complex (EC), a meta-volcano-sedimentary sequence forming the Congo Craton's southern extension (Clifford 1970). The EC is intruded by the Mesoproterozoic Kunene Intrusive Complex (KIC) comprising anorthositic and minor granitic rocks. The KIC is exposed as a N-S elongated intrusion of >300 km in length in SW Angola and, to a lesser extent, in NW Namibia. It was emplaced at ~ 1385 ± 25 Ma to 1347 ± 13 Ma (Mayer et al. 2004; Drüppel et al. 2007). Near Epembe, ~ 50 km southwest of Swartbooisdrift, a large calcite carbonatite dike transects the metamorphic basement, for which a SIMS-Pb-Pb zircon age of 1173 ± 12 Ma was calculated (Simon et al. 2017). Syenite and nepheline syenite of the same area were recently dated by Tshiningayamwe et al. (2022), resulting in U–Pb zircon ages of 1220 ± 3 Ma and 1205 ± 13 Ma, respectively.

The Swartbooisdrift carbonatites intrude the southern margin of the KIC, west of the Kunene River in an area of ~ 100 km^2. They are classified as ferrocarbonatite with mantle-like C–O isotopes (Thompson et al. 2002; Drüppel

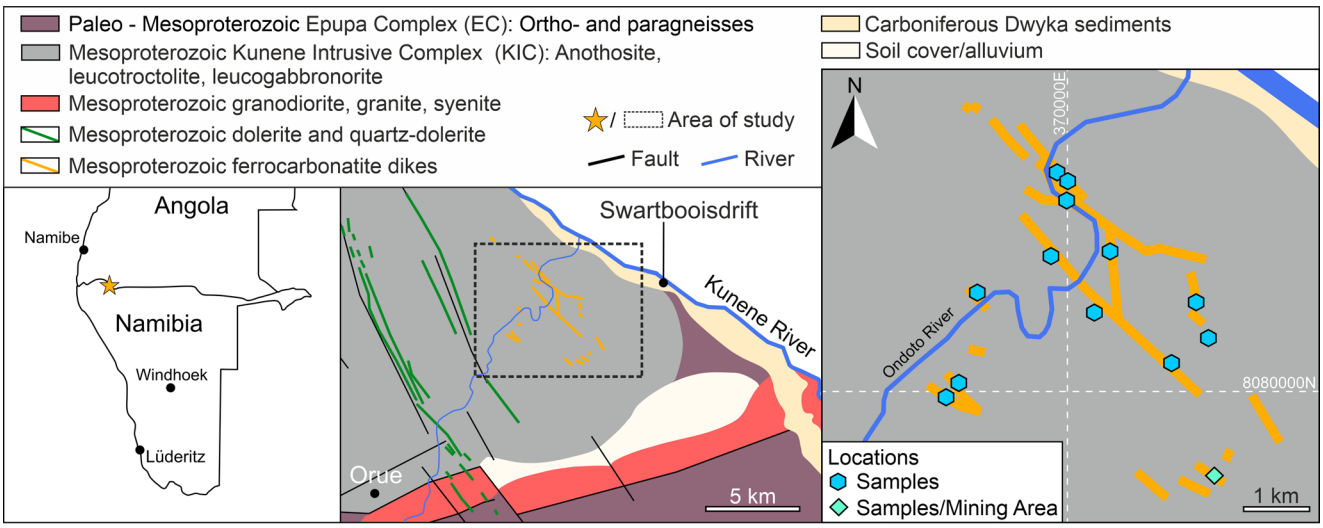

Fig. 1 Simplified geological map: contacts interpreted from Menge (1998). Location markers illustrate main sample locations. Coordinates for each individual sample are documented in ESM2

et al. 2005). U–Pb dating of pyrochlore gave a preliminary age of 1140–1120 Ma (data provided by S. Littmann, in Drüppel et al. 2005). Locally, minor nepheline syenite and lamprophyre dikes are associated with the carbonatite.

Field observations

Mapping and field observations indicate that the zones of weakness, introduced during and after solidification of the anorthosites of the KIC, were reutilized during subsequent intrusions (Drüppel 2003; Drüppel et al. 2005, 2007). The emplacement of the carbonatites (Fig. 2) occurred mainly along NW-SE striking and moderately to steeply (40–64°) SW dipping shear and fault zones. During intrusion of the ferrocarbonatites, the previously emplaced syenite was incorporated as clasts and strongly to completely overprinted (Fig. 3a). Metasomatism also affected the bordering anorthosites leading to the formation of broad, Na-metasomatic fenite aureoles (Drüppel 2003). Carbonatite dikes range between several centimeters up to tens of meters in width and contain abundant fragmented wall rock material and—in places—syenitic clasts. The ferrocarbonatites are fine to very coarse grained and characterized by a brownish weathering color. The following succession of events can be deduced from field relationships: (i) Early sodium-dominated metasomatism (fenitization), described in some detail in Drüppel et al. (2005), leads to the transformation of plagioclase of the surrounding anorthosites into both albite and sodalite (Fig. 3b). During the same event mafic minerals of the anorthosite suite are progressively transformed into Na-amphiboles. These products of the early Na-metasomatism are progressively replaced by muscovite and cancrinite during the hydrothermal stage. (ii) The emplacement of a first generation of carbonatite (FC1) occurred at the same time as the fenitization (Fig. 3b). FC1 is represented by an ankerite- and magnetite-rich carbonatite hosting abundant fenitized anorthosite and syenite xenoliths of mm- to m-scale (Figs. 2a and 3c). Biotite forms along the contacts between FC1 and both xenoliths and bordering wall rock. In places accumulations of homogeneous and small grained biotite-ankerite-magnetite-apatite form. Flow-banded alternations of silicate- and carbonate-dominated layers, sometimes displaying irregular magmatic folding, are common. In the carbonate-rich domains ankerite dominates. Fluorapatite, pyrochlore, magnetite, burbankite, and calcite are minor but can be enriched to form nearly monomineralic

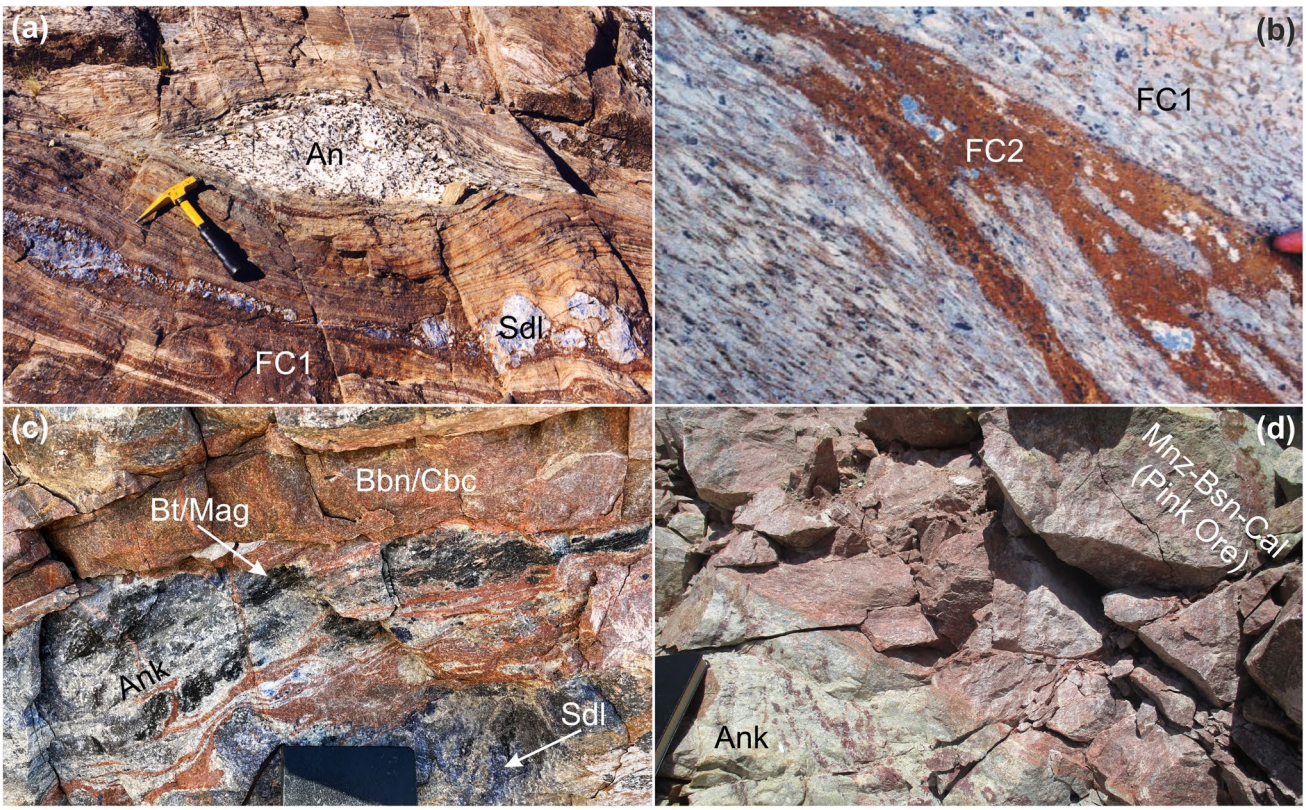

Fig. 2 **a** Brown ferrocarbonatite 1 (FC1) with pale blue sodalite (Sdl), and a white/grey anorthosite-clast (An). Note magmatic folding of the silicate rich FC1. **b** Late stage, brown ferrocarbonatite 2 (FC2) vein intersecting FC1 (grey, blue). **c** Pinkish red burbankite and carbocernaite (Bbn/Cbc) schlieren with white ankerite (Ank), blue sodalite, and black biotite/magnetite (Bt/Mag, black). **d** Massive zone of monazite-bastnäsite-calcite LREE ore (Mnz-Bsn-Cal, Pink Ore) from the mining area hosted in ferrocarbonatite. Ankerite (beige) contains rust-red schlieren of pseudomorphs after primary REE minerals, most likely burbankite and apatite

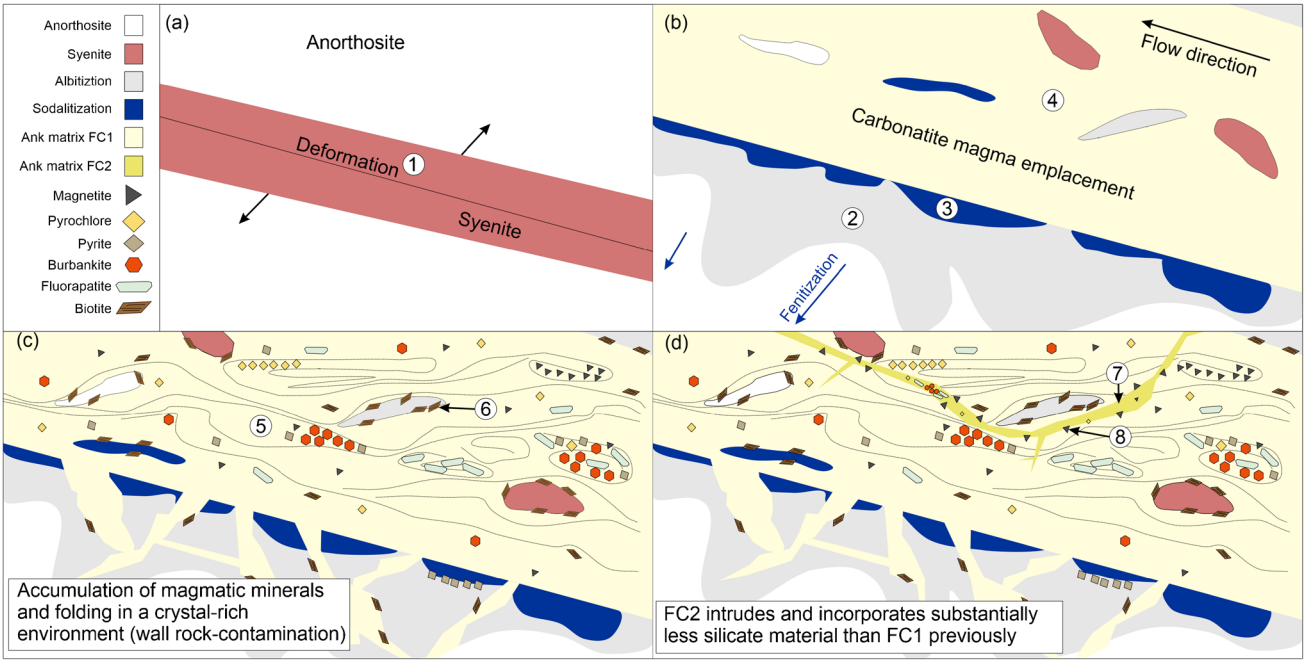

Fig. 3 Schematic overview of the stages of ferrocarbonatite intrusion and associated metasomatism: **a** Simplified setting before ferrocarbonatite emplacement: reactivation of extensional shear zones in anorthosite, which were previously intruded by syenite **(1)**. **b** Emplacement of ferrocarbonatite 1 (FC1) along faults, associated with metasomatic albitization of the wall rocks **(2)**, metasomatic formation of sodalite **(3)** and incorporation of wall rock and fenitized material **(4)**. **c** Crystallization and accumulation of magmatic phases of the ferrocarbonatite (ankerite, fluorapatite, pyrochlore, burbankite) followed by magmatic separation and development of flow banding and magmatic folding **(5).** Biotite forms in FC1 or along contacts between FC1, wall rocks, and xenoliths **(6)**. **d** Intrusion of a second generation of ferrocarbonatite (FC2), which is mostly silicate-free **(7)**. Magnetite forms along FC2 contacts with other lithologies **(8)** instead of biotite (FC1). Mineralogically FC1 and FC2 are almost identical

layers. Irregular sulfide-oxide veins (pyrite–chalcopyrite–magnetite) occur locally where several larger dikes intersect (Drüppel et al. 2006). (iii) A second generation of nearly silicate-free ferrocarbonatites (FC2) intrudes mainly into FC1 and forms cm- to m-sized veins or dikes (Figs. 2b and 3d). Its mineral assemblage is nearly identical to FC1, but FC2 contacts are marked by magnetite rather than biotite.

A regional extent of pinkish calcite-bastnäsite-monazite ore, which is restricted to the carbonatite dikes, was discovered by Ellmies et al. (2021) during exploration. This REE ore is widespread in the eastern part of mining area (Fig. 1). These dike-like REE ore bodies, which are hosted by FC1, reach up to 4 m in width (Fig. 2d) and were termed "pink ore" due to their reddish to pinkish color. The regional and therefore economic scale of the carbonatite-hosted REE-mineralization was first recognized in 2010 during prospecting activities of Kunene Resources (Pty) Ltd. Systematic mapping, geophysics and drilling led to the definition of several REE ore bodies currently under development (open pit mining) by Ondoto Rare Earth (Pty) Ltd. Resource definition drilling with more than 600 boreholes revealed a down-dip extension of the major ore bodies for more than 400 m often forming several subparallel ore bodies resulting in JORC-compliant measured, indicated and inferred resources with ~ 20,000 t total rare earth oxide contained (Ellmies et al. 2023).

Sampling and analytical methods

More than 500 regional samples were investigated petrographically (sampled from 1997 to 2022). From these, 39 samples with abundant REE-bearing minerals were selected and further analyzed.

Whole-rock analyses

All whole-rock analyses were performed at the Institute of Applied Geoscience, Karlsruhe Institute of Technology (AGW-KIT). Semi-quantitative mineral proportions were estimated by powder X-ray diffraction (XRD). Major-element concentrations were determined by wavelength-dispersive X-ray fluorescence (WD-XRF), and loss on ignition (LOI) was measured by mass difference. Trace elements and REE were analyzed by inductively coupled plasma mass spectrometry (ICP-MS) after complete acid digestion. Quality control included certified reference materials (Govindaraju 1994) and blanks. Full instrumental parameters and

reference materials are provided in the Electronic Supplementary Material 1-Sect. 1 (ESM1-S1).

Stable isotopes

Carbon and oxygen isotope ratios ($\delta^{13}C$ and $\delta^{18}O$) were measured on carbonate powders using a GasBench II isotope ratio mass spectrometry (IRMS) system with phosphoric-acid digestion. Data are reported relative to VPDB ($\delta^{13}C$) and VSMOW ($\delta^{18}O$). Accuracy and precision were monitored by repeated measurements of certified reference materials. Analytical precision was 0.05 ‰ for $\delta^{13}C$ and 0.08 ‰ for $\delta^{18}O$. The analyses were performed at the Laboratory for Environmental and Raw material Analysis (LERA), AGW-KIT. See the ESM1-S2 for the full analytical protocol and instrument conditions.

Mineral chemistry

Major-element mineral compositions for ankerite, calcite, pyrochlore, fluorapatite, and carbocernaite were obtained by electron probe microanalysis (EPMA) on polished, carbon-coated sections at the Institute of Mineralogy, University of Würzburg. At AGW-KIT additional EPMA data was acquired on a Jeol JXA 8200 to verify burbankite, monazite and bastnäsite-synchysite-parisite-group minerals, identified by scanning electron microscopy coupled with energy dispersive X-ray analysis (SEM–EDX). Standardless SEM–EDX analyses were applied to REE-(fluor)carbonates and secondary Nb-oxides. SEM was also used for backscattered electron (BSE) imaging. Raman spectroscopy at AGW-KIT was used to differentiate REE-(fluor)carbonates. The identification of minerals was carried out by comparison with spectral databases (RRUFF database; Armbruster and Danisi 2015) using the software CrystalSleuth and Spectragryph (Menges 2024). Cold/hot cathodoluminescence supported interpretation of primary versus secondary mineral growth (AGW-KIT). Trace element concentrations of ankerite, calcite, pyrochlore, fluorapatite, burbankite, and carbocernaite were determined by laser ablation ICP-MS (LA-ICP-MS) at the University of Mainz, Germany using EPMA-derived CaO as internal standard. Full operating conditions, reference materials, interference considerations (Ba–REE peak overlap), and analyte lists are given in the ESM1-S3 to S7. An additional EPMA measurement campaign is planned to deepen the understanding of the complex REE- and F-bearing mineralogy.

Data processing and availability

All REE data (ICP-MS and LA-ICP-MS) were chondrite-normalized, using values from McDonough and Sun (1995). Data handling and plotting of scatter plots, REE chondrite-normalized plots, and ternary diagrams with Python (version 3.12.10) utilized the following libraries: pandas (The Pandas Development Team 2025), matplotlib (Hunter 2007), numpy (Harris et al. 2020) and mpltern (Yuji Ikeda 2024).

Mass balance calculations were made using an excel spreadsheet (EASYGRESGRANT) that was provided by López-Moro (2012). This allowed evaluation of volume, mass and composition changes during REE ore formation. López-Moro (2012) designed this spreadsheet according to Gresens (1967), Kresten (1988) and the summary provided by Grant (2005). Water-immersion specific gravity (SG) measurements for ore samples were provided by Rainer Ellmies. SGs of 3.26 and 3.05 were applied for burbankite-rich zones and pink ore respectively.

Sample information, whole-rock geochemistry, stable isotope data, and mineral chemistry are provided in ESM2. The ESM3 file includes all available Raman data of analyzed minerals. The LA-ICP-MS data and spot locations are given in ESM4 and ESM5, respectively. The results of the mass balance calculations are given in ESM6.

Results

Whole-rock geochemistry

FC1 and FC2 samples with $SiO_2 < 30$ wt.%, (most samples < 4 wt.%) were classified as ferrocarbonatites according to Le Maitre (2002). REE chondrite-normalized plots and scatterplots of FC1 and FC2 are geochemically similar. Small-scale mineral variations lead to steepening/flattening REE curves (Fig. 4a–c). Ferrocarbonatite varieties rich in burbankite with strong REE enrichment (~10 wt.%, $n = 4$) display steeper patterns (~8000 La/Yb CN, $n = 4$). Pink ore samples closely match burbankite-rich zones but have steeper REE-patterns (~14000 La/Yb CN, $n = 6$) and have more total REE (13 wt.%, $n = 6$).

Petrographic features and alteration textures

Ferrocarbonatites (FC1, FC2)

Petrographically, the main difference between FC1 and FC2 is the reduced amount of xenolithic silica material within the latter. Mineral descriptions therefore account for both stages of intrusion. Ankerite forms subhedral, locally recrystallized granular to elongated mosaics (typically cm-scale). Contacts with burbankite, fluorapatite, and magnetite are straight to gently curved; boundaries with pyrochlore are generally straight (Fig. 5). Primary calcite fills interstices

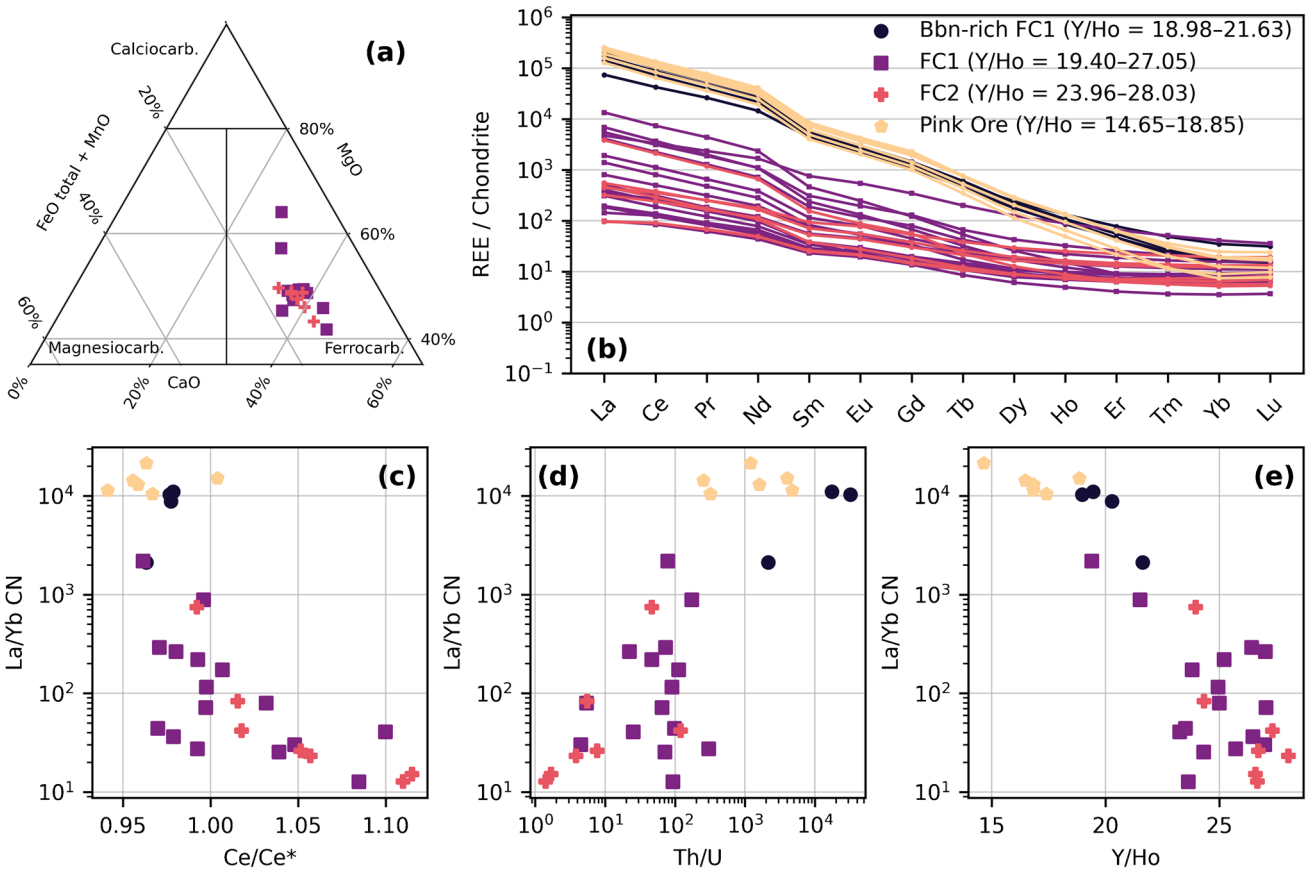

Fig. 4 Whole rock geochemistry of ferrocarbonatite 1 (FC1), ferrocarbonatite 2 (FC2) burbankite-rich zones in ferrocarbonatite 1 (Bbn-rich FC1), and monazite-bastnäsite-calcite-hematite zones (Pink Ore): **a** Ternary carbonatite classification plot from Le Maitre (2002). **b** Chondrite-normalized (McDonough and Sun 1995) REE-Spider plot. **c** La/Yb CN vs Ce/Ce* = Ce CN / √ (La CN * Pr CN). In whole rock carbonatites, Ce/Ce* (cerium anomaly) primarily reflects mineral content and fractionation of Ce-selective phases. Ce anomalies arise because Ce can be stabilized as Ce^{4+} (unlike neighboring LREE) and can partition into specific accessory minerals (e.g. early pyrochlore and apatite). The observed decrease in Ce/Ce* with increasing La/Yb CN is therefore interpreted mainly as progressive fractionation involving early Ce-binding phases in FC1. The last stage of this fractionation is expressed as Bbn-rich FC1 samples. The lowest Ce/Ce* values occur in pink ore zones, consistent with enhanced (hydrothermal) fluid activity and oxidation (hematite-bearing). **d** La/Yb CN vs Th/U and **e** La/Yb CN vs Y/Ho

and is dull yellow with cold-CL. Secondary calcite in veins crosscutting primary fluorapatite is bright yellow (Fig. 5g).

Pyrochlore occurs as disseminated euhedral to subhedral grains or grain clusters (≤150 µm; Fig. 5a-c). It commonly contains inclusions of albite, ankerite, and calcite and is concentrically zoned. Pyrochlore often shows signs of alteration ranging from minor embayment of grain margins to pseudomorphic replacement by secondary minerals like columbite-(Fe) and chlorite. Chlorite is later replaced by natrolite. Columbite-(Fe) has rare inclusions of µm-sized (late, low REE, high Sr) burbankite.

Fluorapatite forms euhedral to subhedral prisms or anhedral grains (~50–500 µm; locally ≤5 mm; Fig. 5d-g) irregularly distributed in the matrix. Primary fluorapatite shows distinct oscillatory zonation with bright blue colors (cold-CL), whereas secondary fluorapatite is less bright, more violet, and shows no zonation (Fig. 5g). Concentric cores are locally overgrown by secondary fluorapatite ± monazite-(Ce). Rare inclusions in fluorapatite comprise burbankite, ankerite, magnetite, and calcite.

Burbankite is unusually well preserved. It occurs as (i) subhedral to anhedral, mm-sized grain clusters, (ii) interstitial subhedral to anhedral grains (10–100 µm), and (iii) anhedral to subhedral burbankite crystals ≤50 µm in diameter in burbankite-fluorapatite rich accumulations (Figs. 5d-f and 6a-d). Rare inclusions of burbankite (10–50 µm) occur in fluorapatite. Five different alteration textures of burbankite were observed:

(i) Carbocernaite I replaces interstitial grains and grain clusters of burbankite. Replacement starts along the cleavage and grain margins of burbankite (Figs. 5 d-f and 6 b-c, f).

(ii) Carbocernaite II + calcite + barite ± strontianite ± hematite replace burbankite and carbocernaite I. Rounded pyrite with µm-scale hematite rims is restricted to texture (ii), implying pyrite formed simultaneously with burbankite and was subsequently oxidized. Unaltered pyrite coexisting with burbankite was not observed (Fig. 6a, c–e).

(iii) Cordylite-(Ce) + barite ± calcite occur in veins crosscut burbankite and form on its grain boundaries (Fig. 6a, d). Cordylite-(Ce) forms euhedral prisms of ~ 10–250 µm replacing burbankite textures (i) and (ii). The original hexagonal shapes of burbankite are partly preserved, even when completely altered to texture (ii). Muscovite and cancrinite can occur together with cordylite-(Ce) at contacts between cordylite and sodalite.

(iv) Monazite-(Ce) (< 5 µm) directly replaces burbankite (Fig. 6b) and carbocernaite I (Fig. 6c) on grain boundaries and cracks.

(v) Ancylite-(Ce) ± calcite ± celestine ± strontianite locally replace burbankite and alteration texture (ii) (Fig. 6e-f). Ancylite-(Ce) is anhedral and < 5 µm partly replacing individual zones of carbocernaite II. Rarely subhedral with grains ≤ 50 µm are observable.

Monazite-bastnäsite-calcite ore

The pink ore occurs as mm- to cm-sized irregular schlieren/veins in ferrocarbonatite and fenite and as massive discontinuous lenses and bands of up to 4 m in width, spatially confined to the ferrocarbonatite dikes (Fig. 7). The main minerals of the pink ore are intergrowths of fine-grained monazite-(Ce), bastnäsite-(Ce) and calcite (Fig. 8). Minor hematite, pyrite, chlorite, barite, strontianite and rare µm-sized relicts of carbocernaite and burbankite are present. The overall texture is often homogeneous and massive. Interestingly, the REE-minerals alignment partly resembles an isometric, apparently hexagonal, and mostly medium-grained precursor mineral. This can be recognized, even though replacement by secondary minerals was pervasive. The intergranular space between these former grains is mainly filled with calcite, hematite, and chlorite.

Calcite of pink ore is mostly subhedral. Grains (> 1 mm in diameter) can reside between pseudomorphs and 10–50 µm crystals form the matrix. Calcite has straight grain boundaries to bastnäsite-(Ce), hematite, and monazite-(Ce). Monazite-(Ce) is subhedral (≤ 45 µm; mostly around 10 µm), bastnäsite-(Ce) is mostly anhedral to subhedral (~ 4–40 µm), minor synchisite-(Ce) (few µm–40 µm) form euhedral overgrowths on the former. Hematite typically forms euhedral to subhedral blades (few µm to ~ 30 µm) and anhedral pseudomorphs after pyrite. Pyrite is generally rare in pink ore and partly to completely replaced by hematite and monazite. Notably, monazite-dominant samples sometimes contain abundant homogeneously distributed euhedral pyrite. Barite and strontianite are anhedral and only found in association with bastnäsite-(Ce). Strontianite is present as inclusions up to 10 µm in bastnäsite-(Ce) or as larger grain accumulations of up to several hundreds of µm in diameter, where it is associated with barite, bastnäsite-(Ce), and calcite. Small calcite crystals of up to 2.5 µm are present in this texture. Ancylite-(Ce) is generally rare and can be found as 10 µm inclusions in bastnäsite-(Ce). Minor anhedral quartz occurs replacing carbonate along crystal lattice planes. Anhedral columbite-(Fe) aggregates up to ~ 100 µm can be found in chlorite veins together with hematite, calcite and monazite-(Ce).

The textural observations imply the following mineral sequence of the pink ore: Pyrite forms before hematite. Monazite-(Ce), partly in stable assemblage with pyrite, forms prior to bastnäsite-(Ce) and synchisite-(Ce). Strontianite, barite, and rare ancylite likely form contemporaneously with bastnäsite-(Ce) and hematite. Calcite is stable throughout the whole crystallization sequence of the pink ore.

C-O isotopes

C-O isotope analyses were performed for ankerite, burbankite (88 vol.% burbankite, 12 vol.% carbocernaite), secondary zones (44 vol.% calcite, 40 vol.% carbocernaite, 16 vol.% celestine) and pink ore (72 vol.% calcite, 15 vol.% bastnäsite-(Ce), 13 vol.% monazite-(Ce)). All samples show compositionally restricted $\delta^{13}C$ (VPDB) values of -7.16 ‰ to -6.84 ‰, which are in a similar range of those reported by Thompson et al. (2002) and Drüppel et al. (2005) for magmatic ankerite. $\delta^{18}O$ (VSMOW) values, on the other hand, increase from primary to subsequently formed secondary carbonate assemblages from ~ 7.6 ‰ (primary ankerite) to ~ 9.4 ‰ (burbankite-carbocernaite) and ~ 10.5 ‰ (pink ore).

Mineral chemistry

Pyrochlore

Besides Nb, EPMA analyses of pyrochlore document SrO (1.0–2.3 wt.%), CaO (11.5–13.9 wt.%), and Na_2O (6.5–8.0 wt.%). The A-site is occupied by almost equal amounts of Ca and Na and only minor Sr. Pyrochlore contains high amounts of Ta (up to 0.9 wt.%) and the LREE (La: 0.4–1.1 wt.%, Ce: 0.8–2.3 wt.%, Nd: 0.2–0.8 wt.%) with the ΣREE ranging between 1.4 and 4.1 wt.%.

Due to its strong alteration and the abundance of mineral inclusions, it turned out to be difficult to analyze pyrochlore with LA-ICP-MS. The chondrite-normalized REE

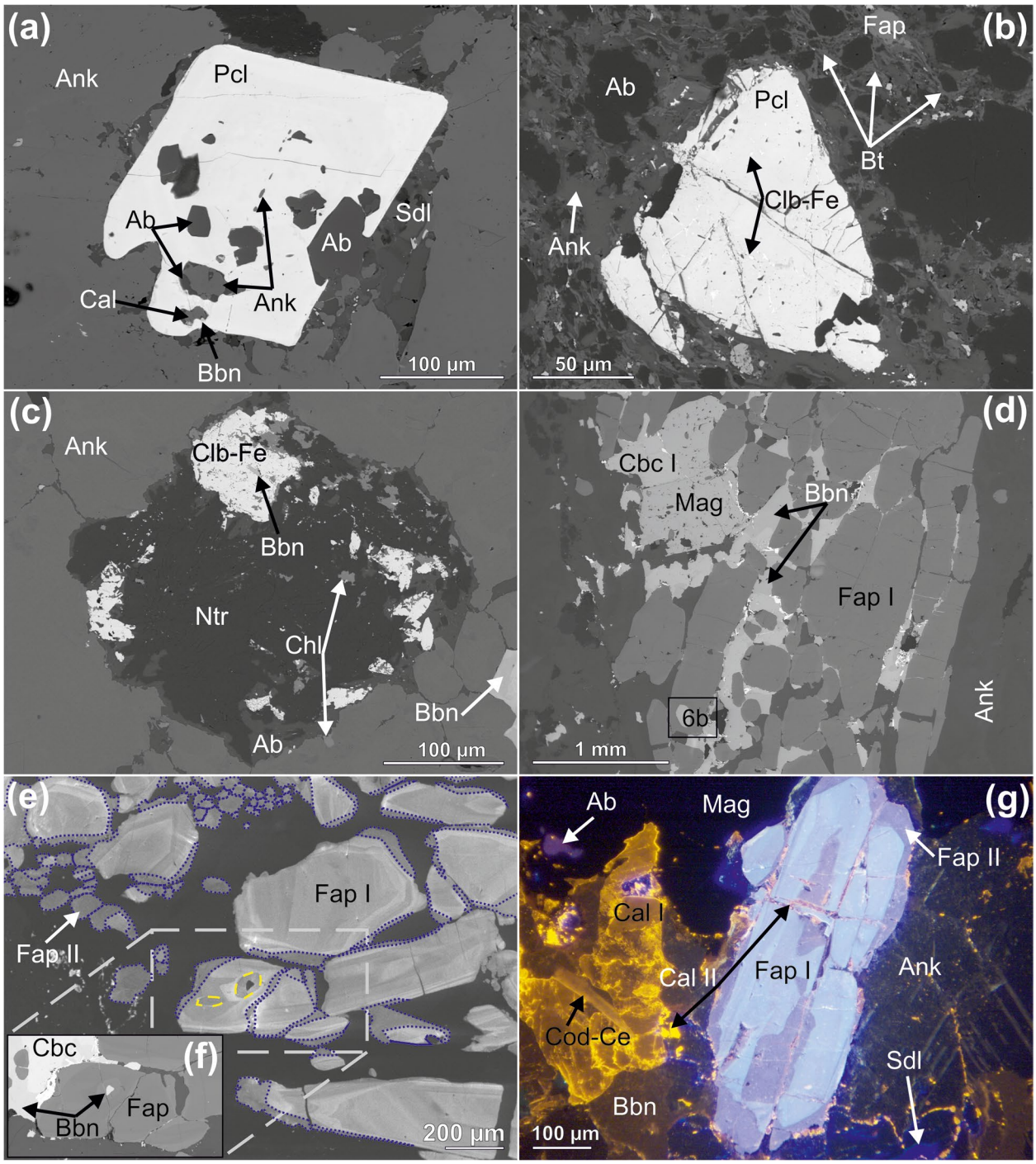

patterns of pyrochlore have steep negative slopes and show the highest Ce/Ce* of all analyzed minerals (~1.2) (Fig. 9). Notables are high U (>1000 µg/g), high ΣREE (>3 wt.%) and near-chondritic Y/Ho ratios (23–24). Interestingly, the REE patterns (Fig. 9) are remarkably similar to those of carbocernaite and burbankite until Dy, where the pyrochlore patterns flatten.

Niobium-oxides

Niobium-bearing secondary minerals form after pyrochlore and can be found in biotite rich-zones in FC1 and pink ore. They are characterized by up to 80 wt.% Nb_2O_5, around 17 wt.% Fe_2O_3, and minor TiO_2 and were identified as columbite-(Fe) by Raman spectroscopy.

Fig. 5 Primary REE- and Nb-minerals in the ferrocarbonatite. SEM-BSE pictures: a-d, f; cathodoluminescence (CL): (e) hot, (g) cold. **a** Primary, concentrically zoned pyrochlore (Pcl) showing inclusions of ankerite (Ank), albite (Ab), and burbankite (Bbn). Sodalite (Sdl) replaces albite. **b** Pyrochlore in layered ferrocarbonatite (FC1) shows signs of deformation and alteration: White spots are late REE-minerals and columbite-(Fe) (Clb-Fe), the matrix is composed of albite and ankerite together with biotite (Bt) and fluorapatite (Fap). **c** Replacement of pyrochlore by chlorite (Chl), columbite-(Fe), and minor albite. Late natrolite (Ntr) replaces chlorite. Low-REE, high Sr-burbankite in columbite-(Fe). **d** Primary fluorapatite (Fap I) prisms, magnetite (Mag), burbankite, and ankerite. Figure 6b shows the inclusion of burbankite in fluorapatite in detail. **e** Primary zoned, euhedral to subhedral fluorapatite from different generations recorded with hot-CL. Darker hot-CL and brighter BSE reflect higher REE. First generation cores marked yellow, with fluorapatite forming around a burbankite inclusion. Note the dark grey hot-CL of first-generation fluorapatite around the burbankite. The boundary between first and second generation fluorapatite (Fap II) is marked with a blue dotted line. Note the brecciation of fluorapatite I and later formation of metasomatic fluorapatite II granules and rims. **f** SEM picture in same scale as (e) to show the subhedral burbankite inclusion in fluorapatite. **g** Cold-CL: bright yellow secondary calcite (Cal II), dull yellow primary calcite (Cal I), cloudy dull yellow cordylite-(Ce) (Cod-Ce), burbankite with hardly any luminescence (only a yellow tint, hard to discern from carbocernaite). Ankerite shows a slight greyish color, primary fluorapatite is bright blue and zoned and secondary fluorapatite is violet-to-blue and unzoned (Fap II). The silicates present are royal blue sodalite and violet albite

Fluorapatite

As determined by EPMA measurements, the primary apatite is classified as a strontian fluorapatite. SrO contents are in the range of 1.1 to 2.5 wt.%. F contents range from 1.3 wt.% to 5.1 wt.%, whereas Cl is subordinate (up to 0.3 wt.%). F contents greater than 3.77 wt.% are likely due to analytical issues related to apatite, commonly leading to unrealistically high values (Goldoff et al. 2012; Stock et al. 2015). F should be regarded as qualitative. Concentrations of Na_2O (0.33–1.09 wt.%) and BaO (0–0.14 wt.%) positively correlate with F. Remarkably, the highest Na contents are recorded by early fluorapatite inclusions in biotite.

Chondrite-normalized REE patterns from LA-ICP-MS (Fig. 9) reveal low La/Yb CN ratios (~61, $n=18$) compared to pyrochlore, carbocernaite, and burbankite (Fig. 9). Y/Ho (~22.8) is below the chondritic value (~28) but still high, Pb/Th is low at ~0.4. Ce/Ce* is ~1.08, which is lower than pyrochlore (around 1.2). Sr is at around 2.3 wt. %, the sum of REE is at ~2 wt.%, and Ba < 50 µg/g. U is mostly below the detection limit. Efforts to date the ferrocarbonatite with fluorapatite accordingly proved to be unsuccessful.

Monazite-(Ce)

Comparison of EPMA trace element data of monazite-(Ce) ($n=25$), grown in the matrix of pink ore or in the vicinity thereof (thin-section scale), with primary apatite show similar Ce/Ce* (~1.09), higher Pb/Th (~5.06; excluding two measurements with Th below the limit of detection), higher LREE at around 59 wt.%, and higher Th (~0.24 wt.%). SrO and CaO range from ~0.2 wt.% to ~1.0 wt.% and U is at or < LOD. Age dating of monazite-(Ce) on EPMA was not successful.

Ankerite-dolomite

Ankerite-dolomite solid solutions are characterized as ankerites in this study if they have a Mg/Fe ratio of < 4 (Deer et al. 1992). Dolomites exist in minor proportions and are mostly Fe-free. FC1 ankerite displays variable compositions, mainly depending on texture. (i) Rare early ankerite inclusions in magmatic magnetite (X_{Mg}: 0.79–0.84) as well as subhedral ankerite of the ferrocarbonatite matrix (X_{Mg}: 0.61–0.77) are characterized by the highest X_{Mg} values. (ii) Anhedral matrix ankerite commonly displays distinctly lower but variable Mg contents (X_{Mg}: 0.25–0.64). Individual grains show decreasing Mg contents from the core towards the rim, whereas both MnO (0.6–2.5 wt.%) and SrO (0.1–0.8 wt.%) increase in the same direction.

FC2 ankerite (X_{Mg}: 0.43–0.64) has a similar Mg/Fe ratio like FC1 matrix carbonates but is characterized by significantly higher MnO contents (2.3–3.4 wt.%). These ankerites are commonly characterized by Fe-rich cores (X_{Mg}: 0.43–0.49) and strongly reversed rims (X_{Mg}: 0.55–0.64). The change from Fe-rich cores to Mg-rich rims is not gradual but with a sharp boundary.

Based on their chondrite-normalized REE patterns, ankerites ($n=29$) can be subdivided into three groups (Fig. 10): (i) steep negative slopes of the REE patterns (Ank in Fig. 10), Y/Ho is around ~22–26, La/Yb CN ~5–16; (ii) negative slope and flattening of the REE patterns (Ank_flat in Fig. 10) towards the HREE, Y/Ho ~25–26, La/Yb CN ~2.8; (iii) flattening of the REE patterns (Ank_lowREE in Fig. 10) towards the HREE ($n=5$), Y/Ho ~23–26, La/Yb CN ~0.7. Ankerite (i) is the most common and builds the matrix of the ferrocarbonatites; (ii) was found in connection with carbocernaite alteration and has the lowest Sr/Ba ratio of all measured ankerites; group (iii) was only recorded in pink ore and the directly bordering ferrocarbonatite. Except for a few outliers the cerium anomaly (Ce/Ce*) is > 1 and around 1.08.

Calcite

Calcite either occurs as a rare interstitial phase between larger ankerite grains or forms part of the secondary pink ore. Primary calcite of the ferrocarbonatite is characterized by high Sr/Mn ratios (MnO 0.2– 0.3 wt.%, SrO 0.7–1.8 wt.%) when compared to ankerite. LA-ICP-MS measurements ($n=2$) of

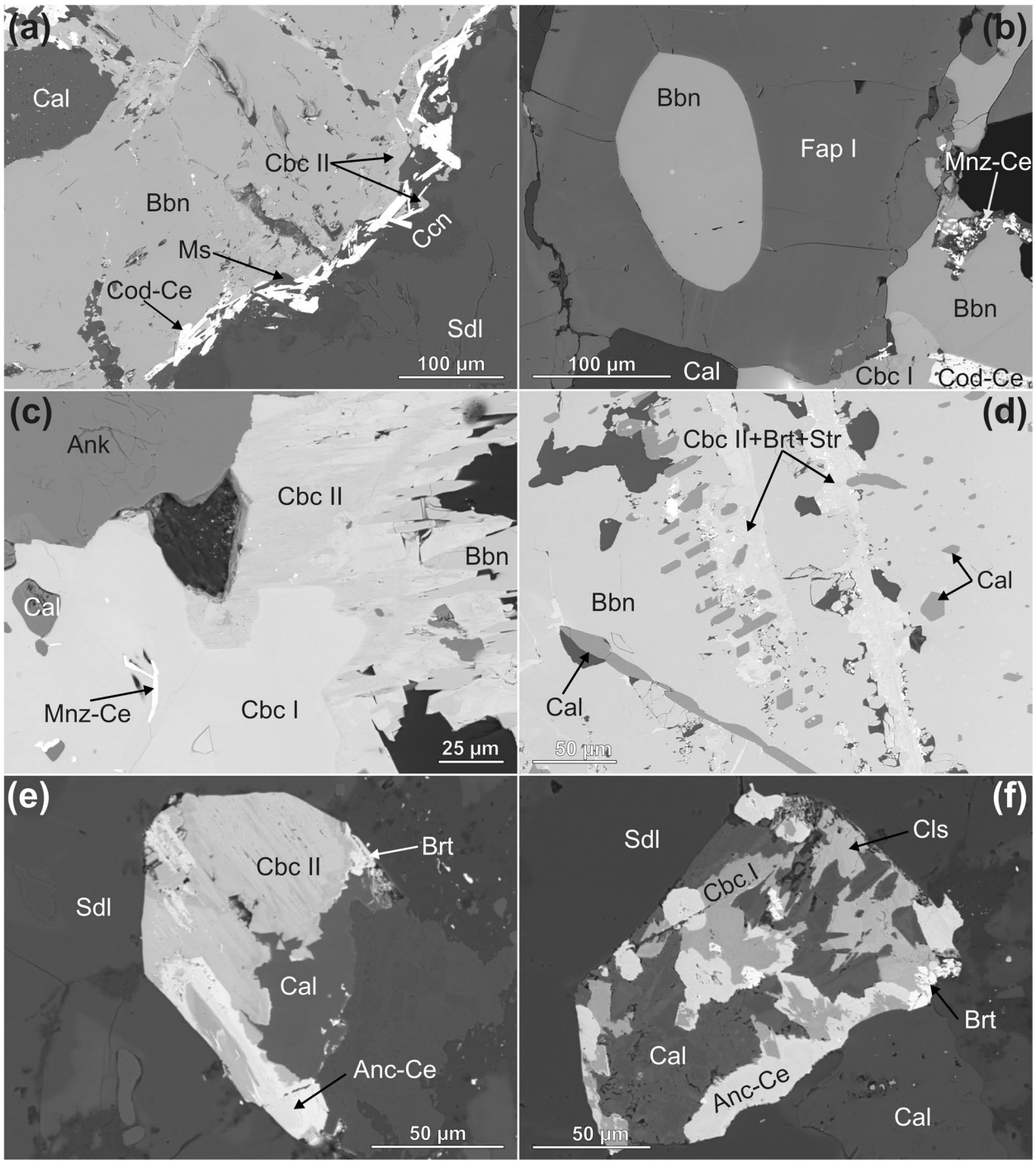

Fig. 6 SEM-BSE images showing replacement textures of primary burbankite (Bbn). **a** Large burbankite grain is successively replaced along cracks and grain boundaries by first stage carbocernaite (Cbc I), second stage carbocernaite II intergrowths (Cbc II), barite (Brt), strontianite (Str) and calcite (Cal), later by cordylite-(Ce) (Cod-Ce), barite, calcite. Texturally late muscovite (Ms) and cancrinite (Ccn) occur in association with cordylite-(Ce) on the boundary between burbankite and sodalite (Sdl). **b** Subhedral inclusion of burbankite in fluorapatite (Fap I). Carbocernaite (Cbc I), cordylite-(Ce), and monazite-(Ce) replace burbankite in the lower left. **c** Burbankite next to ankerite (Ank) is replaced by carbocernaite I, carbocernaite II, barite, strontianite, and calcite. **d** Primary burbankite with aligned idiomorphic inclusions of calcite and carbocernaite I. Burbankite is replaced by carbocernaite II, barite, strontianite, and calcite. **e** Zoned carbocernaite II after burbankite. Carbocernaite II is replaced by ancylite-(Ce) (Anc-Ce), barite, and calcite. **f** Pseudomorph (most likely) after burbankite. Carbocernaite I is replaced by ancylite-(Ce), celestine (Cls), barite and calcite. The pseudomorphic replacements of burbankite e) and f) are situated inside an altered sodalite grain

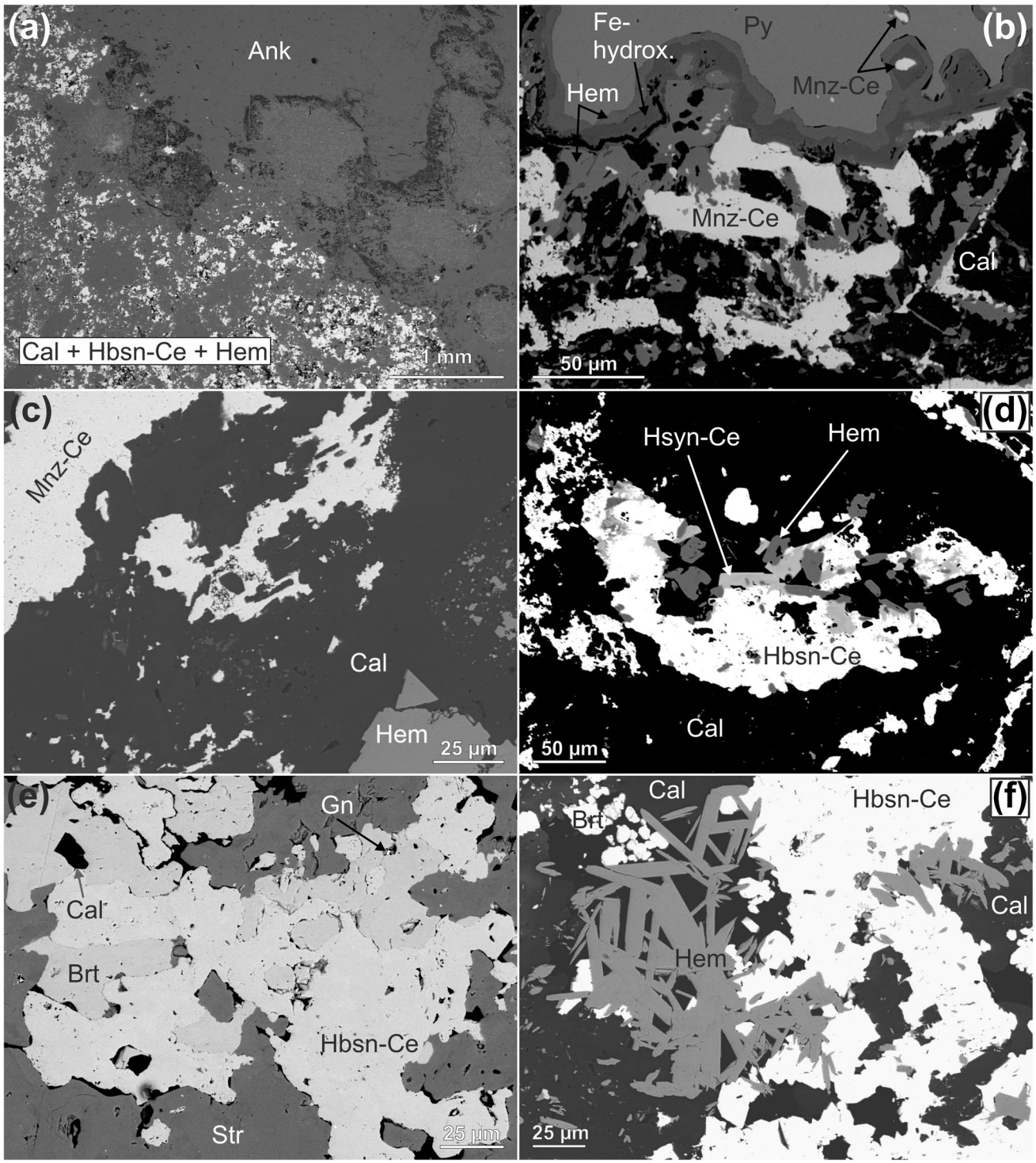

Fig. 7 SEM-BSE images showing REE mineralization in pink ore: **a** Overview of a boundary between pink ore to the left and ankerite (Ank) from ferrocarbonatite to the right. The ore zone in this case composed of calcite (Cal), hematite (Hem) and Hydroxylbastnäsite-(Ce) (Hbsn-Ce). **b** Pyrite (Py) replacement by hematite together with monazite-(Ce) (Mnz-Ce) and calcite. Hematite is further replaced by iron hydroxides (Fe-hydrox.). **c** Ore zone with monazite-(Ce), calcite and hematite. **d** Subhedral hydroxylsynchisite-(Ce) (Hsyn-Ce) overgrowing hydroxylbastnäsite-(Ce) together with subhedral hematite. Calcite defined the matrix of pink ore. **e** Hydroxylbastnäsite -(Ce), barite (Brt), strontianite (Str), calcite paragenesis. Tiny sub µm grains of late galena (Gn) are rarely found. **f** Hydroxylbastnäsit-(Ce) dominated REE ore with calcite, euhedral hematite blades hematite and minor barite

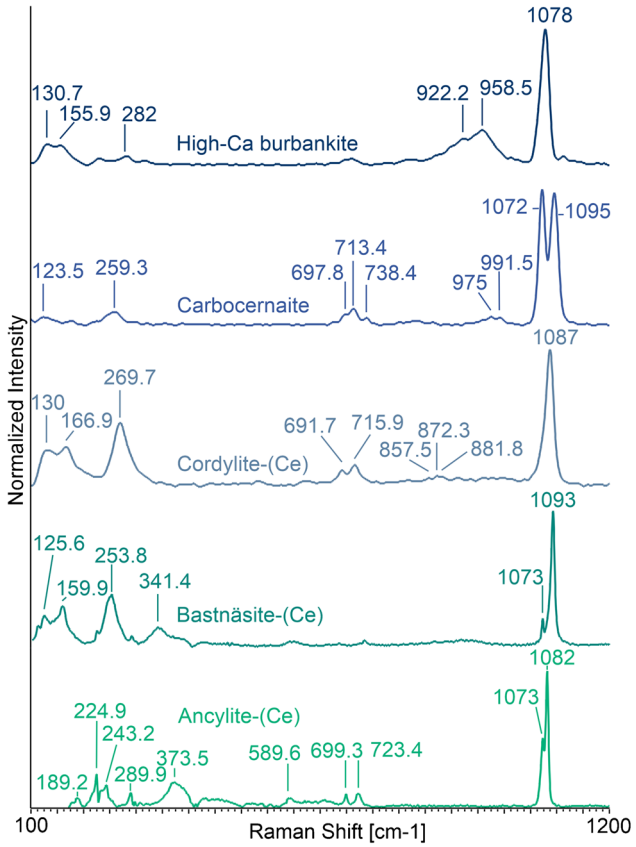

Fig. 8 Representative Raman spectra of high-Ca burbankite, carbocernaite, cordylite-(Ce), bastnäsite-(Ce) and ancylite-(Ce)

calcite from pink ore indicate steeper slopes (La/Yb CN 94 and 251 µg/g) of chondrite-normalized REE patterns than ankerites and Ce/Ce* < 1 (Fig. 10).

Burbankite

Burbankite $(Na,Ca)_3(Sr,Ba,LREE)_3(CO_3)_5$ was identified with Raman (Fig. 8) and analyzed with both SEM–EDX and EPMA, due to its high Na_2O contents. From SEM–EDX analyses the composition of burbankite is variable depending on the sample and to a lesser degree due to its textural occurrence (Table 1). The calculated Na_2O contents are generally high, ranging between 7 to 16 wt.% when compared to CaO (3–16 wt.%). For burbankite of the main ferrocarbonatite body the following trends are observed: negative correlations are evident for ΣREE_2O_3 and Na_2O, BaO and SrO, as well as SrO and CaO.

Sr-dominated burbankite (burbankite sensu stricto) is the prevalent species in FC1. Rarely, interstitial burbankite exhibits high Na and REE > Na. Subordinate high-Ca and REE burbankite, mainly found in REE-rich FC1 samples, has the highest Ba values. In this setting it occurs as euhedral to subhedral crystals, which can reach cm-size. In FC2 burbankite generally has lower ΣREE_2O_3 and high-Sr.

Chondrite-normalized REE patterns from LA-ICP-MS of burbankite ($n = 5$) are characterized by strongly negative slopes with La/Yb CN 32000–52000, Ce/Ce* values of ~ 0.94, and sub-chondritic Y/Ho ratios of ~ 17.3–18.2 (Fig. 9). The sum of REE is ~ 11 wt.%, Ba is around 1.6 wt.%, Sr around 12.7 wt.%, Th around 327 µg/g, Pb at 370 µg/g and U < 1 µg/g.

Table 1 Representative burbankite formulae derived from SEM–EDX measurements

Burbankite	$(Na_{2.7}Ca_{0.3})(Sr_{2.0}REE_{0.8}Ca_{0.1}Ba_{0.1})(CO_3)_5$
High Ca Burbankite	$(Na_{2.1}Ca_{0.5}\square)(Sr_{1.1}REE_{0.9}Ca_{0.8}Ba_{0.2})(CO_3)_5$
High REE Burbankite	$(Na_{2.3}Ca_{0.3}\square)(REE_{1.2}Sr_{1.0}Ca_{0.7}Ba_{0.1})(CO_3)_5$
Low-REE, high-Sr Burbankite	$(Na_{2.1}Ca_{0.9})(Sr_{2.3}Ca_{0.6}REE_{0.1})(CO_3)_5$

Carbocernaite

Carbocernaite $(Ca,Na)(Sr,Ce,Ba)(CO_3)_2$ was distinguished from burbankite by its stoichiometry (lower Na) and the result verified by Raman spectroscopy. Carbocernaite I shows a more restricted range for its elements compared to the chemically zoned carbocernaite II (Fig. 4c-e). The composition of the former can be expressed as $(Ca_{0.6}Na_{0.4})(REE_{0.5}Sr_{0.45}Ba_{0.05})(CO_3)_2$. The composition of carbocernaite II ranges from $(Na_{0.8}Ca_{0.3})(REE_{0.7}Sr_{0.2}Ba_{0.02})(CO_3)_2$ to $Na_{0.1}Ca_{0.9}(Sr_{0.45}Ba_{0.05}REE_{0.5})(CO_3)_2$. On SEM-BSE images carbocernaite with higher Na, Sr and REE content is brighter compared to zones with higher Ca but low in REE and Sr. The zonation visible in Fig. 6c-e reflects these variable contents of Ca and Sr accompanied by increasing values of Na, Ce, and La.

Chondrite-normalized REE patterns from LA-ICP-MS (Fig. 9) of carbocernaite ($n = 9$) are characterized by steep negative slopes with La/Yb CN ~ 18000–46000; Ce/Ce* values are at 0.95, close to those of burbankite, Y/Ho is subchondritic at ~ 17.3–18.8 (Fig. 8). The sum of REE is around 3.5 wt.%, Ba around 0.4 wt.%, Sr at 4.9 wt.%, Th around 115 µg/g, Pb at 51 µg/g, and U < 1 µg/g. The Pb/Th ratio of carbocernaite (0.45) is considerably lower than that of burbankite (1.1).

Ba-REE-F-carbonate

Ba-REE-F-carbonate was identified as cordylite-(Ce) $(NaBaLREE_2(CO_3)_4F)$ by Raman spectroscopy (Fig. 8). From SEM–EDX the composition of cordylite-(Ce) can be approximated with the averaged formula $Na_{0.8}Ba_1(Ce_{0.8}La_{0.7}Nd_{0.2})(CO_3)_4F$. BaO and the REE contents are comparably constant while all other elements show considerable

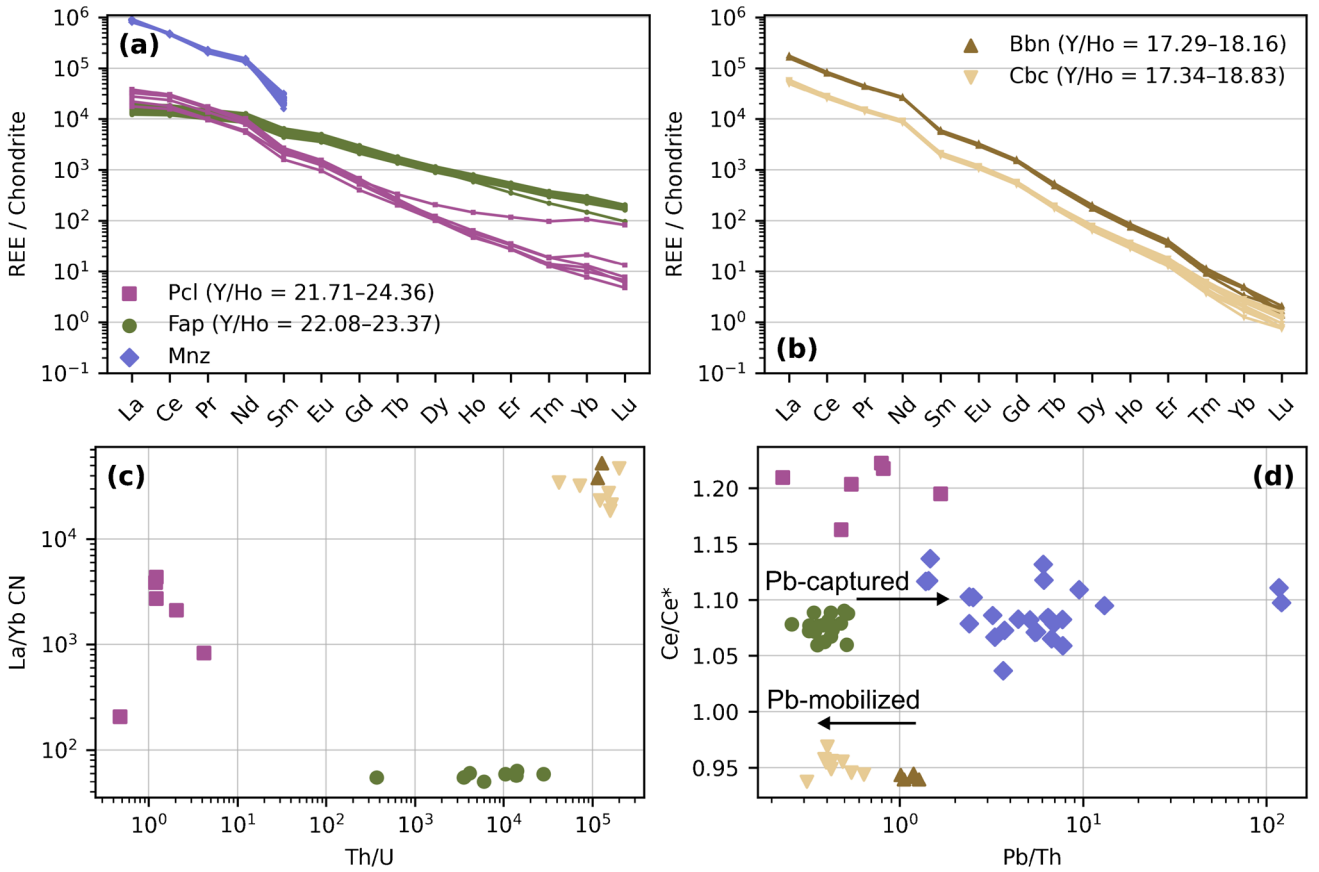

Fig. 9 LA-ICP-MS data for fluorapatite (Fap), pyrochlore (Pcl), burbankite (Bbn), and carbocernaite (Cbc). Trace elements for monazite-(Ce) (Mnz) were determined by EPMA: **a** REE-Spider plot of fluorapatite, pyrochlore, monazite (from La to Sm; Eu to Lu values are near or below the limit of detection (LOD) for the EPMA and therefore omitted from the plot), **b** burbankite, and carbocernaite. **c** La/Yb CN vs Th/U; and **d** Ce/Ce*=Ce CN / √ (La CN * Pr CN) vs Pb/Th. The two right-most monazite markers have Th<LOD. They are plotted at LOD/2 to show the existence of a Th-depleted monazite forming event. Arrows indicate the depletion of Pb when burbankite is transformed into carbocernaite. In contrast monazite forming after apatite has higher Pb/Th-ratios, indicating capturing of Pb in monazite

variations. This initial characterization should be considered as semi-quantitative.

Bastnäsite-Synchysite-Parisite-Group

Bastnäsite, parasite, and synchsite are defined by their Ca/REE ratios, prevalent LREE (La, Ce, Nd), and dominance of F or OH. Bastnäsite is Ca free, parisite has a Ca/REE ratio of 1:2 and synchisite of 1:1. Sub-µm intergrowths can make a clear differentiation difficult. SEM–EDX analyses from FC1 samples suggest the occurrence of F-dominated bastnäsite-(Ce) with Ce>La>Nd. Reliable SEM–EDX analysis for this group of minerals are difficult to attain, due to their CO_2- and F- or OH-rich composition and its close association with other minerals. Bastnäsite-(Ce) was therefore additionally confirmed by Raman spectroscopy (Fig. 8) and EPMA. Raman spectra from FC1 bastnäsite show no signs of OH stretching vibrations around 3200–3800 cm^{-1} as described by Yang et al. (2008).

The available EPMA data of this mineral group from one pink ore sample reveals OH-dominated hydroxylbastnäsite-(Ce) and hydroxylsynchisite-(Ce). The minerals were both analyzes with 1 µm beam diameter which resulted to a lower analytical sum for hydroxylbastnäsite-(Ce) at ca. 90%. The reason is interpreted to be due to damage to the mineral under the measuring conditions. Hydroxylsynchisite-(Ce) has a Ca/REE ratio of 1:1.14, slightly higher than the ideal formula. Thus, hydroxylbastnäsite-(Ce) is likely the main ore mineral in pink ore beside monazite-(Ce).

Ancylite-(Ce)

Ancylite-(Ce) $Sr(Ce,La)(CO_3)_2(OH)$ H_2O shows considerable variability in Ca and Sr contents and to a lesser degree in the REE. The mineral was confirmed by Raman spectroscopy (Fig. 8). The following initial semi-quantitative compositional ranges are determined from SEM–EDX: CaO up to 5 wt.%, SrO from 7 to 19 wt.%, La_2O_3 from 18 to 22 wt.%, Ce_2O_3 from 26 to 30 wt.%, and Nd_2O_3 from 3 to 7 wt.%.

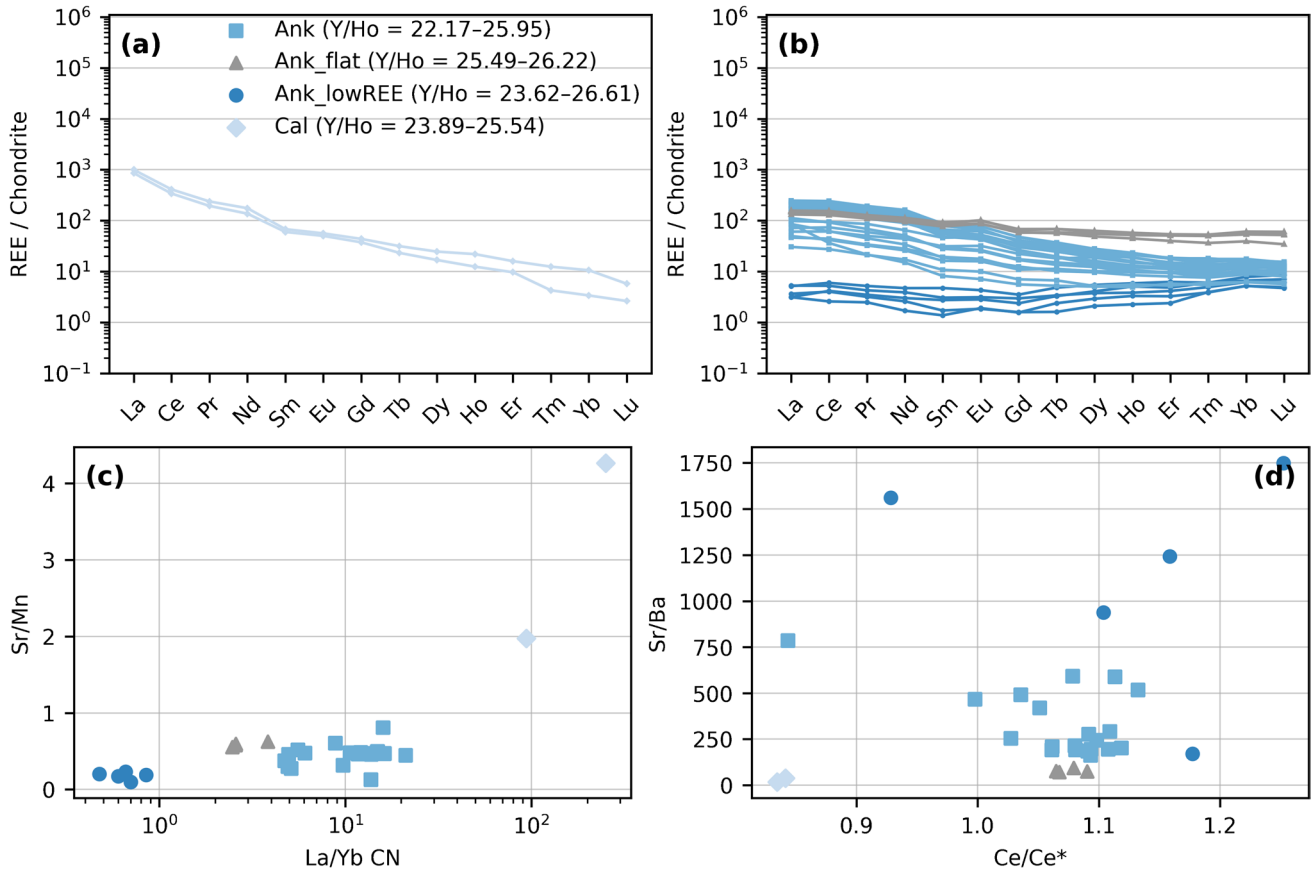

Fig. 10 LA-ICP-MS data for carbonates: **a** Calcite (Cal) and **b** ankerite (Ank) REE-spider plot. **c** Sr/Mn vs La/Yb CN and **d** Sr/Ba vs Ce/Ce* = Ce CN / √ (La CN * Pr CN)

The mineral formula was calculated following the scheme of Dal Negro et al. (1975). Representative formulae can be expressed as $Sr_{0.8}REE_{1.2}(CO_3)_2OH_{1.2} \times 0.8\ H_2O$ and $(Ca_{0.3}Sr_{0.6})REE_{1.1}(CO_3)_2OH_{0.9} \times 1.1\ H_2O$.

Discussion

The combined petrography, geochemistry, mineral chemistry, and C-O isotope data define a magmatic to hydrothermal system. In the following, the datasets are synthesized to track how primary ankerite-magnetite-burbankite-pyrochlore-fluorapatite assemblages were overprinted to form calcite-bastnäsite-monazite ore. The sequence of crystallization as well as the established physicochemical conditions are summarized in Fig. 11.

Magmatic stage

The following early crystallization sequence for the Swartbooisdrift ferrocarbonatites is interpreted from textural relationships and mineral chemistry: Pyrochlore crystallized first, followed by fluorapatite accompanied and outlasted by burbankite, magnetite, and ankerite. Calcite fills interstices. The magmatic character of these phases is inferred from their textural and compositional features.

Early crystallized pyrochlore and fluorapatite are euhedral and show oscillatory zoning, whereas ankerite is concentrically zoned. Crystallization of pyrochlore in ferrocarbonatites is uncommon and rather a typical feature of calciocarbonatites (e.g. Mt Weld, Australia, Chandler et al. 2024). The fact that burbankite occurs as inclusions in or displays straight grain boundaries against these early phases indicates that the Na-Sr-REE carbonate also formed contemporaneously by magmatic crystallization. The crystallization sequence is also supported by Ce/Ce* ratios which show that early pyrochlore (Ce/Ce* around 1.2) preferentially fractionated available Ce^{4+}, followed by fluorapatite (Ce/Ce* around 1.1) with a similar cerium anomaly like ankerite (Ce/Ce* around 1.08), and lastly burbankite with Ce/Ce* around 0.94. In this context Ce/Ce* < 1 is interpreted to be inherited from earlier fractionation of Ce^{4+}.

In most of the samples investigated, burbankite is an accessory phase but it may also form grain accumulations forming discontinuous narrow schlieren or almost monomineralic burbankite layers, following the overall flow-banding

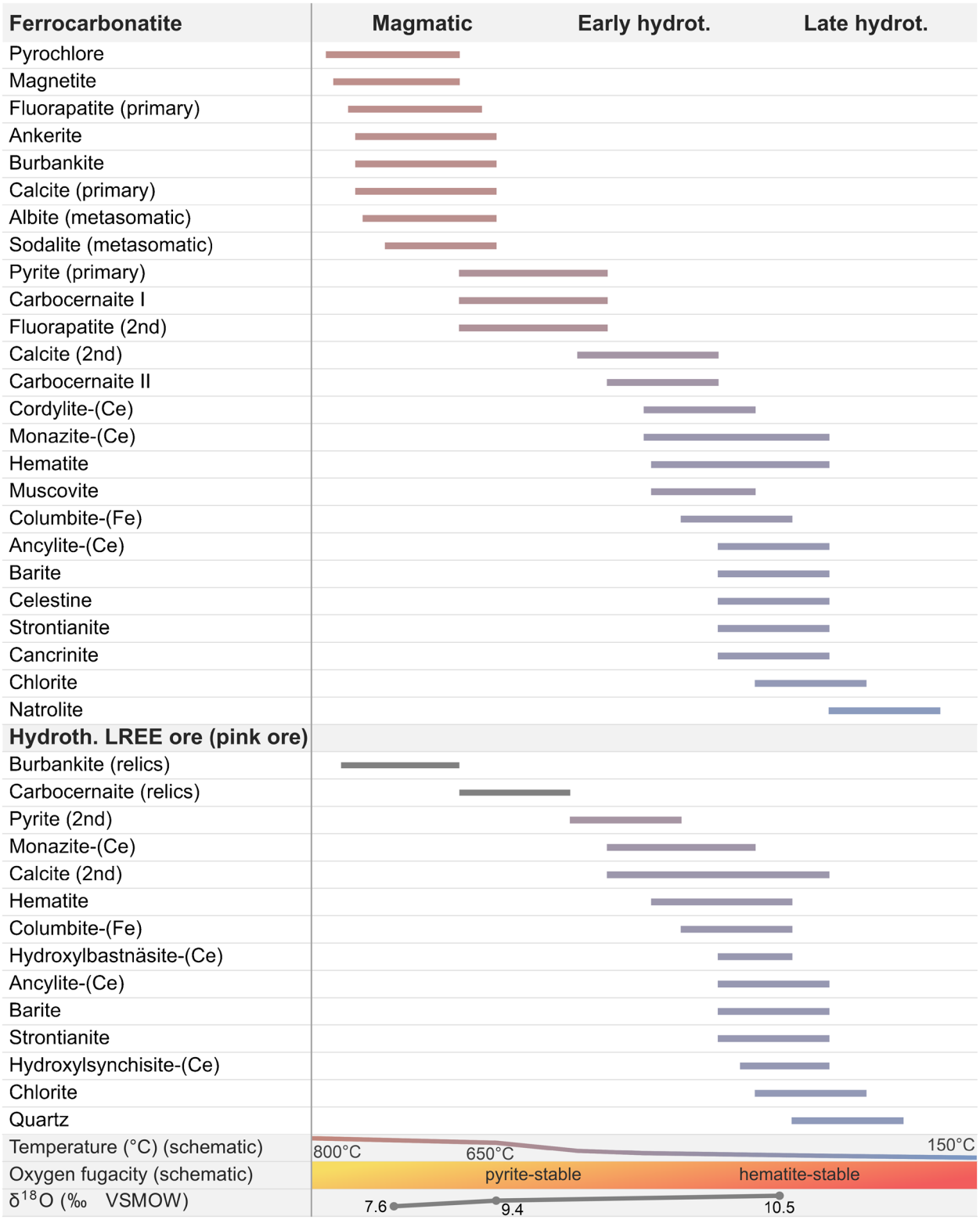

Fig. 11 Paragenetic sequences inferred from textural observations, mineral chemistry, and C–O isotope data. The first sequence depicts the mineral assemblage of magmatic ferrocarbonatite and the effects of successive hydrothermal (hydroth.) overprinting. The second sequence represents the hydrothermal LREE ore (pink ore), which develops when alteration becomes pervasive. At this stage, primary magmatic textures are completely obliterated

structure of the carbonatite. The average modal amount of burbankite is thus difficult to estimate but it can be assumed that, if the whole ferrocarbonatite body is considered, it only occurs in minor to accessory amounts which rarely reach the percentage range. The same holds true for pyrochlore and fluorapatite. The data suggest that pyrochlore, fluorapatite, and burbankite crystallized from a strongly fractionated carbonatite magma, displaying strong enrichment in Fe, Mg, and Ca, but also containing significant amounts of Nb, P, Na, REE, Sr, Ba, and F. The primary Na-rich composition of the ferrocarbonatite magma is moreover confirmed by the presence of broad sodalite-albite-rich fenite aureoles which formed at high temperatures of 700 ± 70 °C (Drüppel et al. 2005).

A magmatic origin of burbankite in carbonatites is suggested by several authors for different carbonatite occurrences but the carbonate is rarely preserved (e.g. Platt and Woolley 1990; Wall et al. 1993, 2004; Zaitsev et al. 2002; Belovitskaya and Pekov 2004; Moore et al. 2015; Dowman et al. 2017, 2023; Chakhmouradian and Dahlgren 2021; Sitnikova et al. 2021). The presented burbankite compositions are within the boundaries of those from other locations as summarized by Chakhmouradian and Dahlgren (2021). In our samples, burbankite is almost exclusively Sr-rich but shows significant chemical variations depending on the composition of the hosting rock and subordinately on textural occurrence. Ca-Ba-rich varieties mainly occur in burbankite grain accumulations, whereas anhedral interstitial burbankite contains high Sr but significantly lower Ba. Belovitskaya and Pekov (2004) point out that a higher Ba content of burbankite in carbonatites is linked to higher crystallization temperatures, whereas high Sr values are reached later in the magmatic evolution, fitting the textural observations of this study. Notably, burbankite only occurs in samples that are poor in silicates like sodalite, albite, and biotite, which formed during carbonatite wall rock interaction and associated Na-Si-metasomatism. Therefore, the controls on the crystallization of magmatic burbankite apparently strongly depend on the amount of Si-assimilation into the carbonatite magma. This observation fits experiments by Anenburg et al. (2020) showing that burbankite forms preferentially in silica-undersaturated environments in a carbonatite magma enriched in alkali elements. The authors observed that with higher (assimilated) SiO_2 of the carbonatite melt, LREE are preferentially bound to fluorapatite (Anenburg and Mavrogenes 2018). In Swartbooisdrift, this assimilation process happens by incorporating material from the surrounding anorthosite suite, syenites, and their already fenitized counterparts into the carbonatite magma.

A temperature of ~ 650 °C for the formation of primary burbankite is inferred from inclusion relationships and an upper temperature suggested for sodalite formation during wall rock fenitization (700 ± 70 °C; Drüppel et al. 2005). Fenitization preceded and outlasted burbankite crystallization. A lower temperature of 460–490 °C for later sulfide veins is indicated based on pyrite-chalcopyrite pairs (Drüppel et al. 2006). These constraints are consistent with the suggestion of Belovitskaya and Pekov (2004) that burbankite in carbonatites forms at T > 500 °C.

Hydrothermal alteration of magmatic REE-minerals

Alteration of the primary magmatic phases starts with waning magmatic conditions and onset of a (hydrothermal) fluid dominated system. Observed textural sequences record progressive Na removal and changing fluid ligands under increasingly oxidizing conditions. All minerals react to these physicochemical changes by releasing Na and altering to secondary minerals.

Alteration of primary fluorapatite leads to formation of secondary granular fluorapatite and narrow fluorapatite rims on early fluorapatite. The secondary origin of these fluorapatite grains is confirmed by their different cathodoluminescence (Fig. 5d), higher REE content, and association with secondary calcite (Fig. 5c) compared to the primary fluorapatite. Additionally, monazite-(Ce) forms along grain boundaries and in close vicinity to all types of fluorapatite.

Pyrochlore alteration is commonly fracture- and margin-controlled and may progress to extensive, locally pseudomorphic replacement by Nb-oxide phases such as columbite-(Fe). Alteration, where Na commonly removed early, is typically hydrothermal and can occur over a range of temperatures from moderate to low during post-magmatic evolution. Associated mineral changes (e.g. chloritization, natrolite) indicate increased H_2O activity during alteration. Na loss is favored when fluid composition maintains low effective Na activity relative to the mineral and promotes cation exchange (Lumpkin and Ewing 1995).

Carbocernaite I replaces burbankite and possibly releases Ba, Sr, Ca and LREE into the fluid to form the next alteration paragenesis. Monazite-(Ce) replaces burbankite and carbocernaite I, demonstrating that the fluid also carries P from fluorapatite dissolution at this stage. LA-ICP-MS data for carbocernaite II zones shows increased Nb and lower LREE values compared to primary burbankite. As Na concentrations further decrease, the alteration assemblages change. Interestingly, there is no Ba-dominated mineral present except for burbankite (~ 1.5 wt.% Ba) until barite and cordylite-(Ce) form. Texturally, both cordylite and barite form after carbocernaite II. Therefore, a hydrothermal process for the formation of secondary Ba-rich phases is inferred rather than a magmatic one. Crystallization of cordylite-(Ce) also marks contribution of F, which is found in primary magmatic pyrochlore and fluorapatite.

The fact that pyrite in close textural relationship with burbankite is replaced by hematite, points to a high oxygen fugacity and mobility of S as $(SO_4)^{2-}$. This interpretation agrees with the findings of Drüppel et al. (2006) that the amount of oxidized S species and thus the oxygen fugacity of the fluid are increasing during the progressive replacement of pyrite in the ferrocarbonatite by secondary sulfide-oxide and finally sulfate-oxide assemblages. Drüppel et al. (2006) explained this trend with mixing of the fenitizing fluid with more oxidizing fluids derived from the host rocks. Together with the textural observations, this suggests that burbankite was primarily replaced by carbocernaite during a change in redox conditions from reducing to more oxidizing. Reducing conditions during burbankite crystallization are supported by its coexistence with pyrite. Initial burbankite alteration marked by carbocernaite I formation might still be connected to the final magmatic stage. The texturally later carbocernaite II, characterized by lower Pb/Th (<0.5) than burbankite (>1), occurs with hematite rims on pyrite, which is consistent with a late-stage oxidizing fluid overprint.

The end-stages of burbankite replacement are marked by the formation of ancylite-(Ce), partly intergrown with celestine. Consistent with this interpretation, low temperatures (<250 °C) are generally assumed for the formation of ancylite (i.e. presence of H_2O and OH^-groups in the formula; Zaitsev et al. 1998). This T estimate also broadly fits to the stability field of celestine in similar rocks (Cangelosi et al. 2020).

Formation of calcite-monazite bastnäsite ore

Where alteration reactions became pervasive along major fluid pathways, they coalesced into the formation of vein- to dike-like pink ore bodies. Several observations suggest that the pink ore formed where burbankite and fluorapatite once were present: (i) Similar key minerals in first and second stage alteration: monazite-(Ce) after fluorapatite and burbankite; (hydroxyl)bastnäsite-(Ce) after burbankite/(possibly) cordylite-(Ce); hematite after pyrite/magnetite; barite, strontianite after burbankite/carbocernaite; chlorite accommodating for Mg and Fe in ankerite; (ii) textural evidence with monazite-bastnäsite-calcite intergrowths (i.e. pink ore) pseudomorphing the shape of accumulations of former medium grained minerals with isometric, hexagonal outline; (iii) its occurrence as vein- or dike-like bodies mainly bound to the ferrocarbonatite. The dominance of monazite-(Ce) and (hydroxyl)bastnäsite-(Ce) over carbocernaite or burbankite, documents the Na-poor environment in which pink ore forms. The abundance of hematite, barite, and strontianite testifies to low temperatures and higher oxygen fugacity during ore formation.

Changes in Y/Ho and Th/U ratios of rocks and minerals (Figs. 4e, and 9a, 10d) can be applied to qualitatively trace REE-enrichment processes and hydrothermal activities since U and Y are more fluid mobile than Th and Ho (Chandler et al. 2024; Reece et al. 2025). Whole rock data of the pink ore has significantly lower Y/Ho and U/Th ratios compared to ferrocarbonatite. Pristine ferrocarbonatite at Swartbooisdrift shows Y/Ho close to chondritic ratios (~24–28). When comparing whole rock REE patterns between burbankite-rich zones in FC1 and pink ore the slope and content of REE partly align. Notably, the pink ore is characterized by slightly higher LREE contents and steeper REE patterns than the burbankite-rich ferrocarbonatite samples. Similar trends can be observed on a mineral basis.

Element mobility during ore formation was assessed using mass-balance calculations (see Methods). For this purpose, the composition of the most burbankite-rich samples was compared to that of the most (hydroxly) bastnäsite-rich pink ore (Supplementary Material 6, Ku-22-06 to TT018d). Elements with similar volume factors, that are suggested to be immobile (Dy, Ho, Cr), were selected for the calculation. Alteration of burbankite-rich zones to pink ore indicates removal of Sr, Na, Mg, Ba and addition of Ca, P, Fe, Mn and LREEs (sum of ~1.2 wt.%). Volume and mass reduction are at 12 vol.% and 17 wt.%, respectively. Pink ore samples with greater abundances of calcite and lesser amounts of (hydroxyl)bastnäsite-(Ce) or monazite-(Ce), REE are reduced compared to burbankite-rich samples (ESM6, Ku-22-06 to TT027 and TT036). Mass balance calculations by Drüppel et al. (2005) demonstrated a similar trend for fenitization that caused increases of Na_2O, CO_2, H_2O, Sr, Ba, Nb and the LREE in the wall rocks. Reactions in the fenite also record the same Na-diminishing reactions with formation of cancrinite and muscovite at a later stage postdating the early metasomatic formation of albite and sodalite.

C-O stable isotope data for separated ankerite and burbankite-carbocernaite accumulations as well as pink ore samples support an interpretation of a mantle source related to primary REE mineralization and subsequent hydrothermal fluid overprint forming the pink ore. The interpretation for burbankite and carbocernaite is difficult due to the limited available data of the acid fractionation factor. C-O stable isotope data of Zaitsev et al. (2002) on burbankite and its pseudomorphs show that unaltered burbankite can retain its magmatic $\delta^{18}O$ with ~7 to 8 ‰ (VSMOW), whereas pseudomorphs record ~11 to 18 ‰ $\delta^{18}O$ (VSMOW). Therefore, the elevated $\delta^{18}O$ values measured for burbankite are best explained by secondary carbocernaite (~12 vol.% in the sample). The $\delta^{18}O$ of burbankite and pink ore indicates the influence of external high-$\delta^{18}O$ fluids, confirmed by textural evidence such as late formation of quartz in pink ore which

is never observed in the primary ferrocarbonatite. This possibly happens when fluids from the surrounding basement infiltrate the carbonatite.

To test whether the inferred fluid transport of REE and partitioning are plausible, experimental data on melt–fluid partitioning and LREE complexation are compared to the findings of this study. Experiments on melt-fluid partitioning of REE, Ba, Sr, Mo and W by Song et al. (2015) indicate that these elements strongly prefer the carbonatite melt over an exsolving hydrothermal fluid. The authors show that F-bearing melt compositions enhance the partitioning of LREE into the melt by a factor of three. This model of primary F enrichment of the melt is supported by the abundance of fluorapatite among the magmatic phases whereas fenitization does not involve the formation of F-bearing phases. Recent experiments indicate that neutral to alkaline fluids can stabilize LREE as CO_3-OH complexes (Nisbet et al. 2022; Reece et al. 2025). This aligns well with the interpretations from this study that show that REE mobility is mainly bound to the ferrocarbonatite itself, whereas only minor LREE mineralization is observed in the bordering fenites. It is the carbonatite supplying the necessary CO_3 for the LREE to stay mobile.

Economic aspects

The pink ore forms the resource base of the Ondoto Rare Earth Mine, currently under construction. The monazite-bastnäsite-calcite ore is remarkably homogenous compared to the primary burbankite-rich zones in the ferrocarbonatite. In-situ pseudomorphic replacement of primary minerals, mobilization and most likely volume and mass reduction upgraded the LREE content. Due to the small size of the cm- to dm-scaled primary burbankite-rich domains, the up to 4 m thick pink ore bodies are the key exploration targets in the Swartbooisdrift mining area. Despite their high LREE concentration, the burbankite-rich zones are only of limited economic interest due to their overall small volume and irregular distribution.

The vein- or dike-like occurrence of the pink ore bodies, together with their high length to width ratio, irregular shape, and overall restriction to large ferrocarbonatite dikes, as well as their abundance where larger ferrocarbonatite dikes intersect, suggest that their formation is structurally controlled and confined to major fluid pathways within the ferrocarbonatite. Despite its heterogeneous distribution in the mining area, the homogeneous character of the ore itself allows simple processing by X-ray transmission sorting and direct acid bake. Additionally, the low Th content of monazite in pink ore (~0.24 wt.%) is beneficiary for downstream handling of concentrates. The observed structural characteristics of the Swartbooisdrift LREE ore resemble those of other LREE deposits like Maoniuping, China (Zheng and Liu 2019), rather than ring structures like Phalaborwa, South Africa (Giebel et al. 2017).

Conclusions

Collectively, the data support an evolution from magmatic crystallization and metasomatism to redistribution of elements and concentration of LREE by hydrothermal alteration. This leads to the progressive transformation of burbankite-bearing ferrocarbonatite into pink ore.

- The Swartbooisdrift ferrocarbonatite dikes feature a strongly fractionated carbonatite composition (i.e., rich in Fe, Mg, Ca, LREE, P, Nb, Sr, Na, Cl, and F) documented by the presence of the magmatic phases ankerite, magnetite, pyrochlore, fluorapatite, and burbankite and associated Na metasomatism (sodalite-albite-rich fenite aureoles)
- The primary REE mineralization is of magmatic origin with burbankite, fluorapatite, and pyrochlore being present in minor amounts but showing a heterogeneous distribution in the ferrocarbonatite, leading to their local concentration
- A late magmatic alteration is superimposed on the magmatic mineral assemblage. REE-minerals that form during this alteration process are carbocernaite, monazite and cordylite. LA-ICP-MS data and C-O isotopes record a fluid dominated system under increasingly oxidizing conditions
- Following this, pervasive pseudomorphic replacement of the previously altered burbankite-rich layers leads to late hydrothermal formation of the monazite-bastnäsite-calcite ore, which mainly occurs inside the ferrocarbonatite dikes as discrete vein- or dike-like bodies. The mineralogy of the pink ore suggests its formation at higher oxygen fugacity and temperatures < 460 °C, post-dating magmatic crystallization, metasomatism, and formation of sulfide veins
- The last stage of the alteration is marked by the formation of texturally late natrolite and associated high-Sr low REE-burbankite, which can be attributed to the circulation of H_2O-CO_2-fluids at very low temperatures of < 150 °C
- Mass balance (volume/mass loss, removal of Sr, Na, Mg, Ba; addition of Ca, P, Fe, LREE) and alteration textures show that within the carbonatite's boundaries LREE can behave mobile. In-situ alteration alone is not sufficient to form the observed mineralization

Supplementary Information The online version contains supplementary material available at https://doi.org/10.1007/s00126-026-01441-8.

Acknowledgements For stimulating discussion and support during field work in 2022 we wish to thank Kaarina Ndalulilwa, and Victoria Haukongo (both Gecko Exploration (Pty) Ltd., Namibia). We are grateful to Kunene Resources (Pty) Ltd for access to the mining area and logistical support. The introduction to the cold cathodoluminescence technique and guidance during data acquisition by Benjamin Busch, Karlsruhe Institute of Technology, Germany, is much appreciated. The support of Ulrich Schüssler during EPMA analysis at the University of Würzburg, Germany is kindly acknowledged. We want to thank Gesine Preus and Dr. Sara Kimmig, Laboratory for Environmental and Raw material Analysis (LERA), Karlsruhe Institute of Technology, for C-O stable isotope analysis and technical advice. We thank Michael Anenburg, Sam Broom-Fendley, an anonymous reviewer, David Banks, and Karen Kelly for their revisions and editorial input on this manuscript.

Author contributions Conceptualization: Albert Riehm, Kirsten Drüppel; Methodology: Albert Riehm, Kirsten Drüppel, Regina Mertz-Kraus; Formal analysis and investigation: Albert Riehm, Kirsten Drüppel, Lars Lenhart, Regina Mertz-Kraus; Writing—original draft preparation: Albert Riehm, Kirsten Drüppel; Writing—review and editing: Albert Riehm, Kirsten Drüppel, Lars Lenhart, Regina Mertz-Kraus, Rainer Ellmies; Visualization: Albert Riehm, Kirsten Drüppel; Data curation: Albert Riehm, Kirsten Drüppel; Funding acquisition: Kirsten Drüppel; Resources: Kirsten Drüppel, Rainer Ellmies; Supervision: Kirsten Drüppel.

Funding Open Access funding enabled and organized by Projekt DEAL. No funding was received for this study.

Declarations

Competing interests The authors have no relevant financial or non-financial interests to disclose.

References

Andersen AK, Clark JG, Larson PB, Donovan JJ (2017) REE fractionation, mineral speciation, and supergene enrichment of the Bear Lodge carbonatites, Wyoming, USA. Ore Geol Rev 89:780–807. https://doi.org/10.1016/j.oregeorev.2017.06.025

Anenburg M, Mavrogenes JA (2018) Carbonatitic versus hydrothermal origin for fluorapatite REE-Th deposits: Experimental study of REE transport and crustal "antiskarn" metasomatism. Am J Sci. https://doi.org/10.2475/03.2018.03

Anenburg M, Mavrogenes JA, Frigo C, Wall F (2020) Rare earth element mobility in and around carbonatites controlled by sodium, potassium, and silica. Sci Adv (Science Advances) 6. https://doi.org/10.1126/sciadv.abb6570

Armbruster T, Danisi RM (2015) Highlights in Mineralogical Crystallography. De Gruyter. https://doi.org/10.1515/9783110417104

Belovitskaya YV, Pekov IV (2004) Genetic mineralogy of the burbankite group

Broom-Fendley S, Styles MT, Appleton JD, Gunn G, Wall F (2016) Evidence for dissolution-reprecipitation of apatite and preferential LREE mobility in carbonatite-derived late-stage hydrothermal processes. Am Mineral 101:596–611. https://doi.org/10.2138/am-2016-5502CCBY

Broom-Fendley S, Wall F, Spiro B, Ullmann CV (2017) Deducing the source and composition of rare earth mineralising fluids in carbonatites: insights from isotopic (C, O, 87Sr/86Sr) data from Kangankunde, Malawi. Contrib Mineral Petrol 172:96. https://doi.org/10.1007/s00410-017-1412-7

Cangelosi D, Broom-Fendley S, Banks D, Morgan D, Yardley B (2020) Light rare earth element redistribution during hydrothermal alteration at the Okorusu carbonatite complex, Namibia. Mineral Mag 84:49–64. https://doi.org/10.1180/mgm.2019.54

Chakhmouradian AR, Dahlgren S (2021) Primary inclusions of burbankite in carbonatites from the Fen complex, southern Norway. Miner Petrol 115:161–171. https://doi.org/10.1007/s00710-021-00736-0

Chandler R, Bhat G, Mavrogenes J, Knell B, David R, Leggo T (2024) The primary geology of the Paleoproterozoic Mt Weld Carbonatite Complex, Western Australia. J Petrol. https://doi.org/10.1093/petrology/egae007

Chikanda F, Otake T, Ohtomo Y, Ito A, Yokoyama TD, Sato T (2019) Magmatic-hydrothermal processes associated with rare earth element enrichment in the kangankunde carbonatite complex, Malawi. Minerals 9:442. https://doi.org/10.3390/min9070442

Clifford TN (1970) The structural framework of Africa. In: Clifford TN, Gass IG (eds) African Magmatism and Tectonics: The structural framework of Africa. Oliver and Boyd, Edinburgh, pp 1–26

Dal Negro A, Rossi G, Tazzoli V (1975) The crystal structure of ancylite,(RE)x,(Ca,Sr)2-x(CO3)2(OH)x(2-x)H2O. Am Mineral 60:280–284

Deer WA, Howie RA, Zussman J (1992) An introduction to the rock-forming minerals, 2nd edn. Longman Scientific & Technical; Wiley, Harlow Essex England, New York NY

Dowman E, Wall F, Treloar P (2023) A comparison of the fenites at the Chilwa Island and Kangankunde carbonatite complexes, Malawi. Mineral Mag 87:300–323. https://doi.org/10.1180/mgm.2022.134

Dowman E, Wall F, Treloar PJ, Rankin AH (2017) Rare-earth mobility as a result of multiple phases of fluid activity in fenite around the Chilwa Island Carbonatite, Malawi. Mineral Mag 81:1367–1395. https://doi.org/10.1180/minmag.2017.081.007

Drüppel K (2003) Petrogenesis of the Mesoproterozoic anorthosite, syenite and carbonatite suites of NW Namibia and their contribution to the metasomatic formation of the Swartbooisdrif sodalite deposits. Doctoral thesis, Fakultät für Geowissenschaften

Drüppel K, Hoefs J, Okrusch M (2005) Fenitizing processes induced by ferrocarbonatite magmatism at Swartbooisdrif, NW Namibia. J Petrol 46:377–406. https://doi.org/10.1093/petrology/egh081

Drüppel K, Littmann S, Romer RL, Okrusch M (2007) Petrology and isotope geochemistry of the Mesoproterozoic anorthosite and related rocks of the Kunene Intrusive Complex, NW Namibia. Precambrian Res 156:1–31. https://doi.org/10.1016/j.precamres.2007.02.005

Drüppel K, Wagner T, Boyce AJ (2006) Evolution of sulfide mineralization in ferrocarbonatite, Swartbooisdrif,Northwestern Namibia: constraints from mineral compositions and sulfur isotopes. Can Mineral 44:877–894. https://doi.org/10.2113/gscanmin.44.4.877

Ellmies R, Haukongo V, Ndalulilwa K (2021) Ondoto LREE-carbonatites, Kunene igneous complex satellite intrusions. SAIMM RARE EARTHS INTERNATIONAL CONFERENCE 2021

Ellmies R, Ndalulilwa K, Kalumbu G (2023) High -grade Rare Earth Carbonatites at Ondoto, Namibia. Colloquium of African Geology, Windhoek, Namibia

Giebel RJ, Gauert CD, Marks MA, Costin G, Markl G (2017) Multistage formation of REE minerals in the Palabora Carbonatite Complex, South Africa. Am Mineral 102:1218–1233. https://doi.org/10.2138/am-2017-6004

Goldoff B, Webster JD, Harlov DE (2012) Characterization of fluorchlorapatites by electron probe microanalysis with a focus on time-dependent intensity variation of halogens. Am Mineral 97:1103–1115. https://doi.org/10.2138/am.2012.3812

Govindaraju K (1994) 1994 compilation of working values and sample descriptions for 383 Geostandards. Geostand Newsl 18:1–158. https://doi.org/10.1046/j.1365-2494.1998.53202081.x-i1

Grant JA (2005) Isocon analysis: a brief review of the method and applications. Phys Chem Earth Parts a/b/c 30:997–1004. https://doi.org/10.1016/j.pce.2004.11.003

Gresens RL (1967) Composition-volume relationships of metasomatism. Chem Geol 2:47–65. https://doi.org/10.1016/0009-2541(67)90004-6

Harris CR, Millman KJ, van der Walt SJ, Gommers R, Virtanen P, Cournapeau D, Wieser E, Taylor J, Berg S, Smith NJ, Kern R, Picus M, Hoyer S, van Kerkwijk MH, Brett M, Haldane A, Del Río JF, Wiebe M, Peterson P, Gérard-Marchant P, Sheppard K, Reddy T, Weckesser W, Abbasi H, Gohlke C, Oliphant TE (2020) Array programming with NumPy. Nature 585:357–362. https://doi.org/10.1038/s41586-020-2649-2

Hunter JD (2007) Matplotlib: a 2D graphics environment. Comput Sci Eng 9:90–95. https://doi.org/10.1109/MCSE.2007.55

International Energy Agency Global Critical Minerals Outlook 2025. https://www.iea.org/reports/global-critical-minerals-outlook-2025. Accessed 6 January 2025. Accessed 6 January 2025

Kresten P (1988) The chemistry of fenitization: examples from Fen, Norway. Chem Geol 68:329–349. https://doi.org/10.1016/0009-2541(88)90030-7

Leible D, Drüppel K (2014) Formation of REE-rich veins in ferrocarbonatite, NW Namibia. Poster

Le Maitre RW (2002) Igneous rocks: A classification and glossary of terms, 2nd edn. Cambridge University Press, Cambridge

Louvel M, Etschmann B, Guan Q, Testemale D, Brugger J (2022) Carbonate complexation enhances hydrothermal transport of rare earth elements in alkaline fluids. Nat Commun 13:1456. https://doi.org/10.1038/s41467-022-28943-z

López-Moro FJ (2012) EASYGRESGRANT—a Microsoft Excel spreadsheet to quantify volume changes and to perform mass-balance modeling in metasomatic systems. Comput Geosci 39:191–196. https://doi.org/10.1016/j.cageo.2011.07.014

Lumpkin GR, Ewing RC (1995) Geochemical alteration of pyrochlore group minerals; pyrochlore subgroup. Am Mineral 80:732–743. https://doi.org/10.2138/am-1995-7-810

Mayer A, Hofmann A, Sinigoi S, Morais E (2004) Mesoproterozoic Sm–Nd and U-Pb ages for the Kunene Anorthosite Complex of SW Angola. Precambrian Res 133:187–206. https://doi.org/10.1016/j.precamres.2004.04.003

McDonough WF, Sun S (1995) The composition of the Earth. Chem Geol 120:223–253. https://doi.org/10.1016/0009-2541(94)00140-4

Menge G (1998) The antiformal structure and general aspects of the Kunene Complex, Namibia. Z Dtsch Geol Ges 149:431–448. https://doi.org/10.1127/zdgg/149/1998/431

Menges F (2024) Spectragryph - optical spectroscopy software. http://www.effemm2.de/spectragryph/

Moore MA, Chakhmouradian AR, Mariano AN, Sidhu R (2015) Evolution of rare-earth mineralization in the Bear Lodge carbonatite, Wyoming: mineralogical and isotopic evidence. Ore Geol Rev 64:499–521. https://doi.org/10.1016/j.oregeorev.2014.03.015

Moshi MC, Watanabe Y, Boniface N, Tsujimori T, Tupaz C, Araoka D, Aoki S, Mshiu EE (2024) Petrological, geochemical and mineralogical characteristics of Wigu Hill carbonatite, Uluguru Mountains, Tanzania: insights into carbonatite evolution and REE mineralization. Miner Deposita 59:1755–1775. https://doi.org/10.1007/s00126-024-01295-y

Nikolenko AM, Stepanov KM, Roddatis V, Veksler IV (2022) Crystallization of bastnäsite and burbankite from carbonatite melt in the system La(CO3)F-CaCO3-Na2CO3 at 100 MPa. Am Mineral 107:2242–2250. https://doi.org/10.2138/am-2022-8064

Nisbet H, Migdisov AA, Goncharov V, van Hinsberg V, Williams-Jones AE, Xu H, Guo X (2022) The solubility and speciation of Nd in carbonate-bearing hydrothermal fluids up to 250 °C. Chem Geol 611:121122. https://doi.org/10.1016/j.chemgeo.2022.121122

Platt RG, Woolley AR (1990) The carbonatites and fenites of Chipman Lake, Ontario. Can Mineral 28:241–250

Reece ME, Migdisov AA, Williams-Jones AE, Strzelecki AC, Waters L, Boukhalfa H, Guo X (2025) Stability of aqueous neodymium complexes in carbonate-bearing solutions from 100–600 °C. Commun Earth Environ 6:1–8. https://doi.org/10.1038/s43247-025-02334-w

Sidorov MY, Kompanchenko AA, Plechov PY, Fomina EN, Kozlov EN (2024) Raman spectroscopy of burbankite group minerals. Zapiski Russian Mineralogical Soc 100–116. https://doi.org/10.31857/S0869605524040077

Simon SJ, Wei C, Ellmies R, Yang H, Soh Tamehe L (2017) New SIMS U-Pb age on zircon from the Epembe carbonatite dyke, NW Namibia: implications for Mesoproterozoic evolution of carbonatites at the southern margin of the Congo Craton. J Afr Earth Sci 135:108–114. https://doi.org/10.1016/j.jafrearsci.2017.08.011

Sitnikova MA, Do Cabo V, Wall F, Goldmann S (2021) Burbankite and pseudomorphs from the Main Intrusion calcite carbonatite, Lofdal, Namibia: association, mineral composition, Raman spectroscopy. Mineral Mag 85:496–513. https://doi.org/10.1180/mgm.2021.56

Song W, Xu C, Veksler I, Kynický J (2015) Experimental study of REE, Ba, Sr, Mo and W partitioning between carbonatitic melt and aqueous fluid with implications for rare metal mineralization. Contrib Mineral Petrol 171. https://doi.org/10.1007/s00410-015-1217-5

Stock MJ, Humphreys MCS, Smith VC, Johnson RD, Pyle DM (2015) New constraints on electron-beam induced halogen migration in apatite. Am Mineral 100:281–293. https://doi.org/10.2138/am-2015-4949

The Pandas Development Team (2025) pandas-dev/pandas: Pandas. Zenodo

Thompson RN, Smith PM, Gibson SA, Mattey DP, Dickin AP (2002) Ankerite carbonatite from Swartbooisdrif, Namibia: the first evidence for magmatic ferrocarbonatite. Contrib Mineral Petrol 143:377–396. https://doi.org/10.1007/s00410-002-0350-0

Tshiningayamwe M, Bolhar R, Nex PA (2022) Petrology, geochemistry and new U-Pb ages of the Epembe syenites and carbonatite, northwest Namibia. J African Earth Sci 196:104719. https://doi.org/10.1016/j.jafrearsci.2022.104719

von Seckendorff V, Drüppel K, Okrusch M, Cook NJ, Littmann S (2000) Oxide-sulphide relationships in sodalite-bearing metasomatites of the Epembe-Swartbooisdrif Alkaline Province, northwest Namibia. Miner Deposita 35:430–450. https://doi.org/10.1007/s001260050254

Wall F, Le Bas MJ, Srivastava RK (1993) Calcite and carbocernaite exsolution and cotectic textures in a Sr,REE-rich carbonatite dyke from Rajasthan, India. Mineral Mag 57:495–513. https://doi.org/10.1180/minmag.1993.057.388.11

Wall F, Mariano AN Rare earth minerals in carbonatites: a discussion centered on the Kangankunde carbonatite, Malawi. In: Jones (Ed.) 1996 – Rare earth minerals, pp 193–225

Wall F, Zaitsev AN, Treloar P (2004) Phoscorites and carbonatites from mantle to mine. Mineralogical Society of Great Britain and Ireland. https://doi.org/10.1180/MSS.10

Wang Z-Y, Fan H-R, Zhou L, Yang K-F, She H-D (2020) Carbonatite-related REE deposits: an overview. Minerals 10:965. https://doi.org/10.3390/min10110965

Yang H, Dembowski RF, Conrad PG, Downs RT (2008) Crystal structure and Raman spectrum of hydroxyl-bästnasite-(Ce), CeCO3(OH). Am Mineral 93:698–701. https://doi.org/10.2138/am.2008.2827

Yuan X, Yang Z, Mayanovic RA, Hou Z (2024) Experimental evidence reveals the mobilization and mineralization processes of rare earth elements in carbonatites. American Association for the Advancement of Science

Yuji Ikeda (2024) yuzie007/mpltern: 1.0.4. Zenodo. https://doi.org/10.5281/zenodo.11068993

Zaitsev AN, Demény A, Sindern S, Wall F (2002) Burbankite group minerals and their alteration in rare earth carbonatites—source of elements and fluids (evidence from C-O and Sr–Nd isotopic data). Lithos 62:15–33. https://doi.org/10.1016/S0024-4937(02)00084-1

Zaitsev AN, Wall F, Le Bas MJ (1998) REE -Sr-Ba minerals from the Khibina carbonatites, Kola Peninsula, Russia: their mineralogy, paragenesis and evolution. Mineral Mag 62:225–250. https://doi.org/10.1180/002646198547594

Zdorik TB (1966) Burbankite and its alteration. Trudy Mineralogicheskogo Muzeya

Zheng X, Liu Y (2019) Mechanisms of element precipitation in carbonatite-related rare-earth element deposits: evidence from fluid inclusions in the Maoniuping deposit, Sichuan Province, southwestern China. Ore Geol Rev 107:218–238. https://doi.org/10.1016/j.oregeorev.2019.02.021